

AEROELASTIC BEHAVIOUR OF A GYROPLANE ROTOR IN AXIAL DESCENT AND FORWARD FLIGHT

J. Trchalík^{*}, E. A. Gillies[†], D. G. Thomson[‡]

^{*} PhD Research Student,
CAA ARB Sponsored 'Aeroelastic Modelling of Gyroplane Rotors'
Research Project, email: jtrchali@aero.gla.ac.uk

[†] Lecturer of Low-Speed Aerodynamics and Aeroelasticity,
email: ericg@aero.gla.ac.uk

[‡] Senior lecturer, Head of the Department,
email: d.thomson@aero.gla.ac.uk

Department of Aerospace Engineering
University of Glasgow
Glasgow, G12 8QQ

Keywords: Gyroplane, autogyro, aeroelasticity, rotor, rotor blade, rotorcraft, stability, axial flight, forward flight

Abstract. A mathematical model was created to simulate aeroelastic behaviour of a rotor during autorotation. Aeroelastic model of a rotor in autorotation (AMRA) captures both bending and twist of the blade and hence it can investigate couplings between blade flapping, torsion and rotor speed. The rotor blades were assumed to be perfectly rigid, i.e. flapping angle and blade twist due to torsion are constant along the blade span. Aeromechanical behaviour of a rotor during both axial flight and forward flight in autorotation were investigated.

Significant part of the research was focused on investigation of the effect of different values of torsional and flexural stiffness of the blade on stability of the autorotation. Special care was taken of mutual relations between blade twist, blade flap and rotor speed. Calculations were carried out for several different positions of centre of gravity in order to determine stability boundary of the rotor. It was found that the aeroelastic behaviour of a rotor in autorotation is affected by strong coupling between blade twist and rotor speed. The results obtained with the aid of the model demonstrate the special characteristics of autorotative regime. Coupled rotor speed/flap/twist oscillations (flutter) occur if torsional stiffness of the blade is lower than a critical value. This instability is unique to the gyroplane as it differs from both helicopter rotor flutter and fixed-wing flutter.

Effects of gust loads on the rotor and corresponding disturbances in flap and twist of the blade were investigated for different blade configurations. In many cases, the results demonstrate auto-stabilizing effect of coupling between blade twist and rotor speed. Parametric studies of influence of gyroplane rotor design on its performance were also accomplished. Simulations were executed for different blade incidence angles and various linear twist of the blade. The effect of blade tip mass and its different location along the blade span on gyroplane rotor performance was investigated also.

NOMENCLATURE

a	Lift-curve slope [1/rad]	T	Blade thrust [N]
a_L	Local lift-curve slope [1/rad]	T	Kinetic energy [J]
A	Rotor disc area [m ²]	U	Inflow velocity [m/s]
AC	Aerodynamic centre	U_p	Vertical component of inflow velocity [m/s]
b	Blade length [m]	U_t	Horizontal component of inflow velocity [m/s]
c	Blade chord [m]	V	Free-stream velocity [m/s]
c_D	Drag coefficient [1]	V	Potential energy [J]
c_L	Lift coefficient [1]	V_d	Speed of descent [m/s]
c_M	Pitching moment coefficient [1]	v_i	Induced velocity [m/s]
c_R	Resultant force coefficient	y_c	Chord-wise offset of aerodynamic centre of the blade from the elastic axis [m]
CG	Centre of gravity	y_g	Chord-wise offset of centre of gravity of the blade from the elastic axis [m]
D	Drag force [N]	α	Blade angle of attack [rad]
EA	elastic axis	α_D	Rotor disc angle of attack [rad]
1/f	Thrust coefficient based on descending velocity [1]	β	Blade flapping angle [rad]
1/F	Thrust coefficient based on resultant air velocity [1]	ϕ	Inflow angle [rad]
G	Gravitational force [N]	γ	Angle of descent/climb of the vehicle [rad]
H	In-plane force [N]	ι	Blade fixed angle of incidence [rad]
L	Lift force [N]	λ, λ_p	Vertical inflow ratio [1]
m	Weight of the blade [kg]	θ	Blade angle of induced twist [rad]
M	Weight of the vehicle [kg]	ρ	Air density [kg.m ⁻³]
M_c	Blade tip mass [kg]	τ	Blade geometric twist [rad]
N_B	Number of blades [1]	τ	Time constant matrix
M_β	Blade forcing moment in flap [N.m]	Λ	Dynamic inflow static gain matrix
M_θ	Blade forcing moment in torsion [N.m]	Ω	Rotor speed [rad]
M_ψ	Blade forcing moment in flap [N.m]	Ψ	Blade azimuth [rad]
Q	Blade torque [N.m]		
R	Rotor radius [m]		
S	Rotor blade area [m ²]		
t	time [s]		

1. INTRODUCTION

The gyroplane represents the first successful rotorcraft design and it paved the way for the development of helicopter during 1940s. Further development of the gyroplane was ceased during following decades as helicopter became more successful. Interest in this type of aircraft was resurrected in recent years thanks to simplicity of its design and low operational costs.

Unfortunately, autogyros, or gyroplanes, have been involved in number of fatal accidents during last two decades¹. Sudden loss of rotor speed or mechanical failures of the rotor blades as delamination were involved in many of the accidents. Very little data on gyroplane flight mechanics and handling qualities are available in the literature. This forced the UK Civil Aviation Authority (CAA) to investigate these problems by contracting the Department of Aerospace Engineering, University of Glasgow to investigate aerodynamics and flight mechanics of a gyroplane.^{1, 2, 3, 4}

The cause of the high accident rate of gyroplanes still remains unclear. Rotor aeroelastic instability has not yet been investigated as a possible cause of some the accidents and it is the aim of the present work to investigate this possibility. This paper shows preliminary results of a CAA funded project on “Aeroelasticity of Gyroplane Rotors”.

The aim of the investigation is to identify flight conditions or configurations of the rotor that might have catastrophic consequences and work out basic design criteria for gyroplane blades. Resulting aeromechanical model of gyroplane rotor blade can be also used for prediction of stability of new or modified gyroplane rotor configurations.

2. DEVELOPMENT OF AN AEROELASTIC MODEL OF GYROPLANE ROTOR

2.1. Overview of the model

There are substantial differences between dynamics of a helicopter rotor and dynamics of a rotor in autorotation. During autorotation, both torque and thrust are generated exclusively by flow through the rotor disc. Thus, in comparison with dynamics of a helicopter rotor, the system has one extra degree of freedom (i.e. rotor speed). Thrust and torque are functions of rotor speed and distribution of local angles of attack along the blade span. Further, angles of attack are dependent upon blade twist, rotor speed, speed of descent and induced velocity. It can be easily shown that both speed of descent and rotor angular velocity are strongly dependent upon rotor torque and rotor thrust. Therefore, simulation of the aeroelastic characteristics of a rotor in autorotation is iterative process that involves large number of algebraic loops. This makes modelling of autorotation significantly more challenging than powered flight.

During steady autorotation, overall torque generated by flow through the rotor disc is zero and rotor thrust is equal to the weight of the vehicle. There are several design parameters of the rotor that determine whether steady autorotation is possible. Perhaps the most important are blade incidence angle (i.e. angle of attack of the blade relative to the rotor disc plane) and blade torsional stiffness. Torque equilibrium can not be achieved for high incidence angles due to high value of blade drag. If torsional rigidity is too low, extensive blade twist has the same effect.

Conditions in which rotor enters autorotative regime are also of great importance. If rotor speed is too low or even zero, the rotor does not autorotate but enters the windmilling regime, requiring pre-rotation to be included in the simulation. A constant value of torque is applied to the rotor in order to reach conditions that make autorotation possible.

Aeromechanical model of autogyro rotor was developed with the aid of *MATLAB – SIMULINK*[®] computer package that offers powerful tools for modelling of complex mechanical systems. The model was named *AMRA*, which stands for ‘Aeroelastic Model of a Rotor in Autorotation’.

A blade element method combined with quasi-steady aerodynamics is used for calculation of aerodynamic forces and moments generated by the rotor blade. Aerodynamic characteristics of the aerofoil for the full range of angles of attack are approximated with the aid of wind tunnel data⁵. NACA 0012 aerofoil was chosen for the first version of *AMRA* model since aerodynamic characteristics for full range of angles of attack of the aerofoil are available⁶. Semi-empirical method of induced velocity calculation was used in the first versions of *AMRA* model. The original calculation⁷ was improved in order to capture blade stall and compressibility of the airflow. Simplified version of Peters - HaQuang inflow model modified by Houston^{8, 9} replaced semi-empirical approach in the later versions of the *AMRA* model in order to improve fidelity of forward flight simulations.

Lagrangian equations of motion were used to describe dynamics of the rotor blade. Adjustable blade incidence (collective pitch in helicopter jargon) and coning angle were incorporated in the dynamic model of the blade. The rotor is assumed to have no lag hinge since it has extra degree of freedom in azimuth. Chord-wise locations of elastic axis (EA), centre of gravity (CG) and aerodynamic centre (AC) can be set in each span-wise station. Values of flexural and torsional rigidity of the blade can be set to investigate behaviour of the rotor for different physical

properties of the blades. AMRA model also allows placement of single concentrated mass at any span-wise station of the blade.

2.2. Aerodynamic model of rotor in autorotation

During autorotation, the flow through the rotor has opposite direction than in the case of powered flight of a helicopter. Thus, blade aerodynamic angle of attack has to be expressed in different form.

$$\alpha_A = \theta + \phi \quad (2.1)$$

Where inflow angle is

$$\phi = \arctg\left(\frac{U_p}{U_T}\right) \quad (2.2)$$

Local values of vertical and horizontal components of inflow velocity (U) have to be calculated in order to determine aerodynamic angle of attack of any blade section. Inflow velocity is a function of angle of attack of the rotor disc that is given by sum of incidence angle of the rotor disc ι (i.e. angle between rotor disc plane and the horizontal) and pitch angle of the vehicle γ (see Eq.(2.3)). During axial flight, rotor disc angle of attack is 90deg.

$$\begin{aligned} \alpha_D &= \iota + \gamma \\ \gamma &= \arctg\left(\frac{V_d}{V_h}\right) \end{aligned} \quad (2.3)$$

Leishman¹⁰ shows that, if quasi-steady flow is considered, lift coefficient of oscillating wing section can be described as follows.

$$c_l \approx a \left[\alpha + \frac{\dot{h}}{V} + \frac{c}{2} \left(\frac{1}{2} - \frac{y_{EA} - \frac{c}{2}}{\frac{c}{2}} \right) \frac{\dot{\alpha}}{V} \right] \quad (2.4)$$

Previous equation can be rewritten so as to describe quasi-steady aerodynamics of a rotor blade more clearly and to match with coordinate system orientation of the model (see Fig.1).

$$c_l \approx a \left[\theta + \phi - \frac{\dot{\beta}r}{\Omega r} - \left(\frac{3c}{4} - y_{EA} \right) \frac{\dot{\theta}}{\Omega r} \right] \quad (2.5)$$

If inflow angles are small, the assumption can be made that $\phi \approx \frac{U_p}{U_T}$. Considering that $U_T \approx \Omega r$, it can be noted that terms on the right-hand side from ϕ can be understood as quasi-steady components of inflow angle. This agrees with the widely used quasi-steady form of blade-

element theory that incorporates the quazi-steady terms into calculations of the inflow angle.¹¹ Referring to Fig.2, if ι is the incidence angle of the rotor disc, the angle between the blade longitudinal axis and the horizontal plane can be expressed as^{10, 12}

$$\iota_b = \beta - \iota \cos \psi \quad (2.6)$$

Therefore, the vertical component of the inflow velocity can be expressed as

$$U_p = V_d \cos(\beta - \iota \cos \psi) + V_h \sin(\beta - \iota \cos \psi) \cos \psi - v_i \cos \beta - \dot{\beta}r - \dot{\theta} \left(\frac{3}{4}c - y_{EA} \right) \cos \theta \quad (2.7)$$

The horizontal component of inflow velocity is given by the following equation

$$U_t = (V_h \cos \iota - V_d \sin \iota) \sin \psi + \Omega r \cos \beta - \left(\frac{3c}{4} - y_{EA} \right) \dot{\theta} \sin \theta \quad (2.8)$$

Component of inflow velocity that is tangential to the rotor disc and parallel with blade axis is usually neglected, especially if axial flight is considered. It is given below.

$$U_r = V_h \cos(\beta - \iota \cos \psi) \cos \psi + V_d \sin(\beta - \iota \cos \psi) - v_i \sin \beta \quad (2.9)$$

The above equations describe inflow velocity components for general flight conditions and they were used in AMRA model of a gyroplane rotor. However, the equations can be modified and simplifying assumptions can be made when describing axial flight or high speed forward flight.

In axial flight, horizontal speed is negligible and $\alpha_D = \gamma = \frac{\pi}{2} \text{rad}$. Thus, $\iota = \alpha_D - \gamma = 0$.

$$\begin{aligned} U_p &= V_d \cos \beta - v_i \cos \beta - \dot{\beta}r - \dot{\theta} \left(\frac{3}{4}c - y_{EA} \right) \cos \theta \\ U_t &= \Omega r \cos \beta - \left(\frac{3c}{4} - y_{EA} \right) \dot{\theta} \sin \theta \\ U_r &= V_d \sin \beta - v_i \sin \beta \end{aligned} \quad (2.10)$$

If both flapping angle and pitch angle of the blade are small, equations (2.10) can be rewritten.

$$\begin{aligned} U_p &= -v_i + V_d - \dot{\beta}r - \dot{\theta} \left(\frac{3}{4}c - y_{EA} \right) \\ U_t &= \Omega r - \dot{\theta} \left(\frac{3c}{4} - y_{EA} \right) \\ U_r &= V_d \beta - v_i \beta \end{aligned} \quad (2.11)$$

Components of inflow velocity can be expressed in different if following substitutions are made¹³

$$x = \frac{r}{R} \quad \lambda = \frac{V_d - v_i}{\Omega R} \quad y = \frac{1}{R} \left(\frac{3}{4} c - y_{EA} \right) \quad (2.12)$$

$$\frac{V}{\Omega R} \cos \alpha_D = \mu \Rightarrow \mu \Omega R = V \cos \alpha_D$$

Hence, equations (2.11) can be written in different form.

$$U_p = \Omega R \left(\lambda - \frac{\dot{\beta}}{\Omega} x - \frac{\dot{\theta}}{\Omega} y \right)$$

$$U_t = \Omega R \left(x - y \frac{\dot{\theta}}{\Omega} \theta \right) \quad (2.13)$$

$$U_r = \Omega R \lambda \beta$$

Above equations can be further modified with the aid of the equation below

$$\frac{1}{\Omega} \frac{d}{dt} = \frac{dt}{d\psi} \frac{d}{dt} = \frac{d}{d\psi} \quad (2.14)$$

Using the above transformation, we get

$$U_p = \Omega R \left(\lambda - \frac{d\beta}{d\psi} x - \theta \frac{d\theta}{d\psi} y \right)$$

$$U_t = \Omega R \left(x - \theta \frac{d\theta}{d\psi} y \right) \quad (2.15)$$

$$U_r = \Omega R \lambda \beta$$

In case of high speed forward flight, rotor disc incidence (ι) is very small and hence the assumption can be made that $\alpha_D \approx \gamma$. Therefore, equations (2.7), (2.8) and (2.9) can be rewritten in the following manner

$$U_p = V_d \cos \beta + V_h \sin \beta \cos \psi - v_i \cos \beta - \dot{\beta} r - \dot{\theta} \left(\frac{3}{4} c - y_{EA} \right) \cos \theta$$

$$U_t = V_h \sin \psi + \Omega r \cos \beta - \dot{\theta} \left(\frac{3}{4} c - y_{EA} \right) \sin \theta \quad (2.16)$$

$$U_r = V_d \sin \beta + V_h \cos \beta \cos \psi - v_i \sin \beta$$

Since rotor disc incidence is negligible, horizontal and vertical components of free-stream velocity are $V_h = V \cos \alpha_D$ and $V_d = V \sin \alpha_D$. Further simplifications in the above equations can be made with the aid of the assumption that flapping angle (β) and blade twist (θ) are small.^{11,14,15}

$$\begin{aligned}
U_p &= V_d - v_i - \dot{\beta}r - \dot{\theta} \left(\frac{3}{4}c - y_{EA} \right) + V\beta \cos \alpha_D \cos \psi \\
U_t &= \Omega r - \dot{\theta} \left(\frac{3}{4}c - y_{EA} \right) \theta + V \cos \alpha_D \sin \psi \\
U_r &= V_d \beta + V_h \cos \psi - v_i \beta
\end{aligned} \tag{2.17}$$

Ignoring negligible terms, it follows from (2.12), (2.7) and (2.8) that ^{11, 15}

$$\begin{aligned}
U_p &= \Omega R \left(\lambda - \frac{x}{\Omega} \dot{\beta} - \frac{y}{\Omega} \dot{\theta} + \mu \beta \cos \psi \right) \\
U_t &= \Omega R (x + \mu \sin \psi) \\
U_r &= \Omega R (\lambda \beta + \mu \cos \psi)
\end{aligned} \tag{2.18}$$

Transformation shown in (2.14) yields in the equations below ^{14, 15}

$$\begin{aligned}
U_p &= \Omega R \left(\lambda - x \frac{d\beta}{d\psi} - y \frac{d\theta}{d\psi} + \mu \beta \cos \psi \right) \\
U_t &= \Omega R (x + \mu \sin \psi) \\
U_r &= \Omega R (\lambda \beta + \mu \cos \psi)
\end{aligned} \tag{2.19}$$

Simplified equations (2.17), (2.18) and (2.19) are frequently used in open literature (see Ref. 11, 14 and 15).

Once both components of inflow velocity (U) are computed at each span-wise station, span-wise distributions of inflow angle and blade aerodynamic angle of attack can be obtained from equation (2.1). Consequently, local lift, drag and pitching moment coefficients at each station can be determined. In early versions of the AMRA model, aerodynamic coefficients were derived from look-up tables of experimental measurements of the aerodynamic characteristics of NACA 0012 for full range of angles of attack.¹⁶ In the later versions of the AMRA model, the look-up tables were replaced with polynomial approximations introduced by Prouty.⁵ Lift, drag and moment coefficients are expressed as functions of Mach number and angle of attack. Therefore, this approach incorporates compressibility effects into the calculations. Figures 3 and 4 show trends of lift coefficient and drag coefficient of NACA 0012 obtained with the aid of Prouty's polynomial approximation.

When the values of aerodynamic coefficients at all span-wise stations are obtained, the forces generated by the blade can be calculated.

$$dL = \frac{1}{2} c_L \rho U^2 c dx \quad dD = \frac{1}{2} c_D \rho U^2 c dx \quad dM_{c/4} = \frac{1}{2} c_M \rho U^2 c^2 dx \tag{2.20}$$

It can be seen from equations (2.10) that inflow velocity does not depend upon azimuth in axial flight. This symmetry makes modelling of axial flight much easier since model of single blade

can be created and resulting aerodynamic forces can be obtained by multiplying of blade lift, drag and pitching moment by number of blades (N_B).

$$L = N_B L_{Bl} \quad D = N_B D_{Bl} \quad M_{c/4} = N_B M_{c/4,Bl} \quad (2.21)$$

In forward flight, inflow angle of the blade is a function of azimuth. Therefore, assumption of uniform rotor disc loading cannot be made.

$$L = \sum_{l=1}^{N_B} L_{Bl}(\psi) \neq N_B L_{Bl} \quad D = \sum_{l=1}^{N_B} D_{Bl}(\psi) \neq N_B D_{Bl} \quad M_{c/4} = \sum_{l=1}^{N_B} M_{c/4,Bl}(\psi) \neq N_B M_{c/4,Bl} \quad (2.22)$$

2.3. Inflow model

Many models of helicopter aerodynamics utilise momentum theory for computation of induced velocity. However, for small negative values of speed of climb, momentum theory fails to estimate induced velocity correctly (see Fig.5). Therefore, classical momentum theory cannot be used for calculation of induced velocity of autorotating rotor.

i) Axial flight

Early versions of the AMRA model used a semi-empirical method computation of induced velocity.⁷ The model uses combination of classical theory of blade aerodynamics and experimental data to estimate values of both induced velocity and speed of descent from the value of vertical component of inflow velocity (U_p). The original method published in Ref. 7 was improved in order to include the effects of blade stall and compressibility.

The relationship between speed of descent and vertical component of speed of descent is given by empirical relation of thrust coefficient based on resultant air velocity $\frac{1}{F}$ and thrust coefficient based on descending velocity $\frac{1}{f}$.

$$\begin{aligned} \frac{1}{F} &= \frac{2\pi R^2 \rho U_p^2}{T} \\ \frac{1}{f} &= \frac{2\pi R^2 \rho V_d^2}{T} \\ \frac{f}{F} &= \left(\frac{U_p}{V_d} \right)^2 \end{aligned} \quad (2.23)$$

Several experimental measurements of these coefficients were carried out and the results published in open literature.^{7, 9, 10, 11} Data from these experiments are summarised in Fig.6. Full-scale experimental results from NACA Technical Note no. 2474¹³ were used in the AMRA model.

It can be shown⁷ that U_p can be calculated with the aid of vertical inflow ratio.

$$u_p = \Omega R \lambda_p = V_d - v_i$$

$$\lambda_p = \frac{-\frac{a_L \theta}{3} + \sqrt{\left(\frac{a_L \theta}{3}\right)^2 - 4 \left(\frac{a_L}{2} - \frac{c_{De}}{2}\right) \left(-\frac{c_{De}}{4} - \frac{2Q}{N_B \rho \Omega^2 R^4 c_e}\right)}}{a_L - c_{De}} \quad (2.24)$$

While linear lift curve and a parabolic drag curve were used in the original semi-empirical method, an approach that allows capture of the effects of blade stall was developed and used in the model. The constant lift-curve slope, which was used in Ref. 7, was replaced by ‘local’ lift curve slope (a_L) and parabolic approximation of drag curve was substituted for value of c_D obtained from experimental data. Local lift curve slope represents slope of imaginary linear lift curve that contains the point $[\alpha_i, c_{L,i}]$. The variable does not have any physical significance and it is merely used to introduce stall effect into the inflow model.

$$a_{L,i} = \frac{c_{L,i}}{\alpha_i} = f(\alpha) \quad (2.25)$$

Figure 7 shows that different value of a_E is allocated to each point of lift curve ($a_L \equiv a$ before stall if the blade section is symmetrical). Since step size of the simulation is very low, this approach induces much lower error than linear lift curve approach.

ii) Forward flight

Since the above semi-empirical inflow model was developed for modelling of axial autorotative flight, alternative inflow model had to be used for forward flight simulation. Modified version of Peters – HaQuang inflow model that was introduced by Houston^{8,9} was used instead. Induced velocity is resolved into three components.

$$v_i = v_{i0} + x v_{is} \sin \psi + x v_{ic} \cos \psi \quad (2.26)$$

These components of the induced velocity are calculated from the following system of differential equations.^{8,9}

$$[\tau] \begin{bmatrix} \dot{v}_{i0} \\ \dot{v}_{is} \\ \dot{v}_{ic} \end{bmatrix} + \begin{bmatrix} v_{i0} \\ v_{is} \\ v_{ic} \end{bmatrix} = [\Lambda] \begin{bmatrix} T \\ L \\ M \end{bmatrix} \quad (2.27)$$

Matrix τ is the time constant matrix^{8,9} and is defined as

$$[\tau] = \begin{bmatrix} \frac{4R}{3\pi V_T C_0} & 0 & \frac{-R.tg\left(\frac{\chi}{2}\right)}{12u_m} \\ 0 & \frac{64R}{45\pi u_m (1+\cos\chi)} & 0 \\ \frac{5R.tg\left(\frac{\chi}{2}\right)}{8V_T} & 0 & \frac{64R.\cos\chi}{45\pi u_m (1+\cos\chi)} \end{bmatrix} \quad (2.28)$$

Whilst matrix Λ is defined as the dynamic inflow static gain matrix and is given by ^{8,9}

$$[\Lambda] = \begin{bmatrix} \frac{R}{2V_T} & 0 & \frac{15\pi.tg\left(\frac{\chi}{2}\right)}{64u_m} \\ 0 & -\frac{4}{u_m (1+\cos\chi)} & 0 \\ \frac{15\pi.tg\left(\frac{\chi}{2}\right)}{64V_T} & 0 & -\frac{4\cos\chi}{u_m (1+\cos\chi)} \end{bmatrix} \quad (2.29)$$

In the equation (2.27) T, L and M are rotor thrust, rolling moment and pitching moment. If V_x , V_y and V_z are component free-stream velocities, the remaining variables from equation (2.27) are given as follows. ^{8,9}

$$\begin{aligned} u_m &= \frac{V_x^2 + V_y^2 + (2u_{mom} - V_z)(u_{mom} - V_z)}{V_T} \\ V_T &= \sqrt{V_x^2 + V_y^2 + (V_z - u_{mom})^2} \\ u_{mom} &= \sqrt{\frac{T}{2\rho A}} \\ \chi &= \tan^{-1}\left(\frac{\sqrt{V_x^2 + V_y^2}}{u_{mom} - V_z}\right) \\ C_0 &= \frac{8}{3\pi} \end{aligned} \quad (2.30)$$

From the system of equations (2.27), only first equation was used in the simulation and the remaining two components of induced velocity were assumed to be negligible. This modification decreases computing time and reduces complexity of the AMRA model significantly. The equation below shows solution for the rate of change of vertical component of induced velocity.

$$\dot{v}_{i0} = -\frac{3C_0 \left(2\pi\rho R^2 v_{i0} \sqrt{V_x^2 + V_y^2 + V_z^2} - \sqrt{2}V_z \sqrt{\frac{T}{\pi\rho R^2}} + \frac{T}{2\pi\rho R^2} - T \right)}{8\rho R^3} \quad (2.31)$$

Hence, the value of induced velocity during forward autorotative flight can be obtained by integration of the above equation according to time.

$$v_i \approx v_{i0} = \int \dot{v}_{i0} dt \quad (2.32)$$

2.4. Blade dynamics

The rotor blades are modelled as perfectly rigid beam, which means that both flap and twist of the blade are constant along the blade span. The blade has three degrees of freedom – in flap, torsion and rotor speed. Lagrangian equations of motion were used for the dynamic model of the blade. The system of equations consists of three differential equations that describe dynamic behaviour of the blade in pitch (twist), flap and rotation. General arrangement of blade equation motion is shown below.

$$\begin{aligned} \frac{d}{dt} \left(\frac{\partial T}{\partial \dot{\beta}} \right) - \frac{\partial T}{\partial \beta} + \frac{\partial V}{\partial \beta} &= M_\beta \\ \frac{d}{dt} \left(\frac{\partial T}{\partial \dot{\Omega}} \right) - \frac{\partial T}{\partial \psi} + \frac{\partial V}{\partial \psi} &= M_\psi \\ \frac{d}{dt} \left(\frac{\partial T}{\partial \dot{\theta}} \right) - \frac{\partial T}{\partial \theta} + \frac{\partial V}{\partial \theta} &= M_\theta \end{aligned} \quad (2.33)$$

In the above equations, T is blade kinetic energy and V is potential energy of the blade and M_β , M_ψ and M_θ are forcing moments. The potential energy of the blade consists of a component due to flexibility of the blade (V_F) and a component due to mass of the blade (V_M). Span-wise mass distribution of the blade was assumed to be homogenous during derivation of the equations of motion. Hence, T and V of a gyroplane rotor having weight m, length b, flexural stiffness k_β , torsional stiffness k_θ and offset of elastic axis from centre of gravity y_g are as follows.

$$\begin{aligned} T &= \frac{m}{2b} \int_0^b \dot{r} \cdot \dot{r} dr \\ V &= V_F + V_M \\ V_F &= \frac{1}{2} k_\beta \beta^2 + \frac{1}{2} k_\theta \theta^2 \quad V_M = \frac{mg}{R} \int_0^R y_g (1 + \sin \theta) dr + \frac{mg}{R} \int_0^R r (1 + \sin \beta) dr \end{aligned} \quad (2.34)$$

After integration, equations describing kinetic and potential energy of the blade give

$$\begin{aligned}
T &= \frac{1}{6}mb^2\dot{\beta}^2 + \frac{1}{2}my_g^2\dot{\theta}^2 - \frac{1}{2}mby_g\dot{\beta}\dot{\theta}\cos\theta + \frac{1}{2}my_g^2\dot{\beta}^2\sin^2\theta - my_g^2\Omega\dot{\beta}\sin\theta\cos\theta\cos\beta + \\
&\quad - my_g^2\Omega\dot{\theta}\sin\beta + \frac{1}{2}mby_g\Omega\dot{\beta}\sin\beta\cos\theta + \frac{1}{2}my_g^2\Omega^2(\cos^2\theta + \sin^2\beta\sin^2\theta) \\
&\quad - \frac{1}{2}mby_g\Omega\dot{\theta}\sin\theta\cos\beta + \frac{1}{6}mb^2\Omega^2\cos^2\beta + \frac{1}{2}mby_g\Omega^2\sin\beta\cos\beta\sin\theta \\
V &= \frac{1}{2}(k_\beta\beta^2 + k_\theta\theta^2) + mg\left(\frac{R}{2}(1 + \sin\beta) + y_g(1 + \sin\theta)\right)
\end{aligned} \tag{2.35}$$

Both blade kinetic energy and the final form of Lagrange's equations of motion were verified with the aid of MAPLE[®] and MATLAB[®] software packages. Forcing moments of the blades are computed from the output of the aerodynamic model of the blade. Each blade is divided into ten span-wise elements and aerodynamic forces and physical properties of the blade are defined in the middle of each element (see Fig.8). Thrust, in-plane force, torque and pitching moment of the j-th span-wise blade element can be calculated using equations below. Boundaries of the element of the blade are defined by dimensionless span-wise coordinates x_{j-1} and x_j . Variable y_c is the offset of aerodynamic centre of the blade element from its centre of gravity and R is blade length (i.e. radius of the rotor).

$$\begin{aligned}
dT_j &= dL_j \cos\phi + dD_j \sin\phi \\
dH_j &= dL_j \sin\phi - dD_j \cos\phi \\
dQ_j &= R\left(\frac{x_j + x_{j-1}}{2}\right)dH_j \\
dM_j &= \left(\frac{y_{cj} + y_{c,j-1}}{2}\right)(dL_j \cos\alpha + dD_j \sin\alpha) - dM_{c/4,j}
\end{aligned} \tag{2.36}$$

Using the variables defined in the previous equation, forcing moments in system of equations (2.33) are

$$\begin{aligned}
M_\beta &= R\sum_{j=1}^n\left(\frac{x_j + x_{j-1}}{2}\right)dT_j \\
M_\psi &= \sum_{j=1}^n dQ_j \\
M_\theta &= \sum_{j=1}^n dM_j
\end{aligned} \tag{2.37}$$

3. EXPERIMENTAL MEASUREMENTS OF BLADE PROPERTIES

Since majority of gyroplane rotor blades are manufactured by small private companies, it is relatively difficult to get any information of structural properties of these blades. A couple of blades from the Montgomerie-Parsons autogyro were subjected to a series of experiments in order to assess its physical properties and mass distribution. Data gathered during the experiments were used as input values of the simulations.

The first blade was cut up into 20 sections and each was measured and weighed so as to ascertain span-wise mass distribution of the blade. Chord-wise position of centre of gravity was also estimated for each blade element from the arrangement of internal structure of each blade section (i.e. position and size of the spar, thickness of the skin and distribution of potential filling material).

Figure 9 shows the internal structure of the blade at blade root and at the tip. It can be seen that both mass distribution and chord-wise positions of CG are mainly given by span-wise distribution of the spar. Span-wise distributions of blade mass and CG locations that were obtained from the experiments are depicted in Fig.10 and Fig.11.

Experimental measurements accomplished with use of second Montgomerie-Parsons autogyro rotor blade were focused on structural properties of the blades. Torsional stiffness and chord-wise positions of elastic axis of the blade were measured at three span-wise stations. Span-wise positions of these the stations were $x = 0.25$ (quarter-span), $x = 0.5$ (half-span) and $x = 0.75$. The rotor blade was firmly fixed at the root and clamped into outboard clamp at the appropriate span-wise station. The outboard clamp was then used for loading of the blade with a torsional moment. Constant weight was used and loading moment was changed by shifting of the weight along the clamp arm. Consequent measurements of blade angular deflections allowed calculation of appropriate stiffness coefficients.

$$k_{\theta} = \frac{M_{\theta}}{\theta} \quad (3.1)$$

Angular deflections of the blade in pitch were determined with the aid of calibrated angle measuring instruments that was fixed to the upper surface of the clamp. The arrangement of the equipment during the experiment is shown in Fig.12. Measurements were carried out for different values of torque at each span-wise station to increase higher accuracy of stiffness estimation. Graphical interpretations of the results are given in Fig.13. Torsional stiffness was determined for each span-wise station of the blade (see the table below).

Span-wise station [1]	0.25	0.5	0.75
Location of EA [%c]	35.5	25.3	27.24
GJ [N.m²/rad]	1534	1443	1409

Table 1 – Locations of elastic axis and torsional stiffness as obtained during the experiment.

Measurement of the first flexural natural frequency of the blade was used to estimate flexural stiffness of the blade. Determination of blade flexural stiffness that was used during the experiment is described below.

$$\begin{aligned}
 f &= \frac{1}{T} = \frac{N_{cycles}}{t} \\
 \omega &= 2\pi f \\
 EI &\approx \frac{\omega^2 R^3 \int_0^1 mx^4 dx}{4}
 \end{aligned}
 \tag{3.2}$$

Data gathered during the experiment are shown in the table below.

Number of oscillations	Time [s]	T [s]	f [Hz]	ω [rad/s]
60	47.63	0.793833	1.25971	7.914993
60	47.62	0.793667	1.259975	7.916655
60	47.67	0.7945	1.258653	7.908352

Table 2 – Characteristics of oscillations in flap of Montgomerie-Parsons rotor blade.

The resulting estimated value of flexural stiffness is $EI = 1166.2 \text{ N.m}^2$.

4. SIMULATION OF AUTOROTATIVE AXIAL FLIGHT

4.1. Initial observations and verification

Series of simulations of aeromechanical behaviour of a gyroplane rotor in axial autorotative flight was performed. The input parameters of the simulations can be found in Table 3.

PARAMETER	VALUE
Blade length (R)	3.63m
Blade chord (c)	0.2m
Chord-wise position of EA (y_{EA})	0.08m = 40%c
Chord-wise position of CG (y_{CG})	0.066m = 33%c
Chord-wise position of AC (y_{AC})	0.05m = 25%c
Offset of CG from EA (y_g)	0.014m
Offset of AC from EA (y_c)	0.03m
Blade weight (m)	13kg
Number of blades (N_B)	2 (but just 1 modelled – assumption of symmetry)
Blade fixed incidence angle	0 rad
Span-wise distribution of blade geometric twist	$\epsilon = 0$ rad
Weight of the autogyro (M)	400kg
Blade torsional stiffness coefficient (k_θ)	1600N.m ² /rad
Blade flexural stiffness coefficient (k_β)	1200N.m ²
Blade section geometry	NACA 0012
Torque used for pre-rotation (Q_{PR})	2000N.m

Table 3 – Input parameters of the simulations.

Simulations of a gyroplane rotor in steady autorotative descent have revealed that the AMRA model captures all key features of the system. The rotor speed has to be increased by application of external torque during pre-rotation. Once the rotor speed reaches sufficient value, the external torque is removed and the system enters autorotative regime. Both acceleration of the rotor from lower rotor speed and transition from helicopter regime (i.e. deceleration from higher rotor speed, see Fig.14) can be demonstrated by the simulation (see Fig.15). Note that rotor speed always stabilises at the same value once steady autorotation is established since its configuration did not change.

It should be noted that rotor speed in autorotation is much lower than rotor speed of helicopter rotor during flight. It can be seen from Fig.14 that the rotor speed is stabilized and the system reaches torque equilibrium within few seconds. At this point, the total thrust of the rotor is in balance with the weight of the vehicle and the value of speed of descent is approximately 11.5m/s (see Fig.16). The value of speed of descent agrees with the results of experimental flight measurements that were carried out by NACA and several other research bodies.^{10,12} The equation below shows empirical relationship of disc loading of an autogyro and speed of descent that was derived from the experimental results.^{10, 12}

$$V_d \approx 1.212\sqrt{T/A} \quad (4.1)$$

Weight of the vehicle is $M = 400\text{kg}$ and rotor radius is $R = 3.63\text{m}$, hence rotor disc loading is $T/A = 96\text{N.m}^{-2}$ and equation (4.1) gives speed of descent $V_d = 11.8\text{m/s}$.

A characteristic span-wise distribution of blade torque for a rotor in the autorotative regime is observed. The inboard part of the blade generates positive torque and the outboard part of the

blade generates negative torque. In steady autorotation, the total value of torque generated by the blade is zero. Figure 17 shows a comparison of span-wise distribution of torque obtained from the simulation and torque distribution as described in open literature.^{10, 12}

The so-called coefficient of resultant force is another important characteristic of autorotative regime.^{10, 12} It is defined by

$$\begin{aligned} c_R &= \frac{2R}{\rho V^2 A} \\ R &= \sqrt{L^2 + D^2} \\ V &= \sqrt{V_h^2 + V_d^2} \end{aligned} \quad (4.2)$$

Previous research involving experimental flight measurements^{10, 12} found that c_R on typical rotor of an autogyro during steady autorotative flight at large rotor disc angles of attack ($\alpha_D > 30\text{deg}$) is about 1.25. It is important to realize that the majority of gyroplane rotors have very small or zero fixed blade angle of incidence (in effect a collective pitch setting, in helicopter jargon). The value of c_R is different for non-zero blade angles of incidence as it is shown later in this paper. Figure 18 shows a comparison of experimental values of c_R ^{10, 12} and the outcome of the simulation. The AMRA model predicts value of c_R to be 1.19.

4.2. Parametric studies

A series of parametric studies of basic rotor designs were undertaken in order to gain more knowledge about the influence of different design parameters of a gyroplane rotor on its performance.

i) Blade fixed incidence

Experimental investigations of gyroplane aerodynamics revealed that range of blade fixed incidence angle (collective pitch), for which steady autorotation is sustainable, is limited.^{10, 12} Results obtained from the AMRA model correlate with conclusions of experimental measurements. The model shows that excessive values of blade collective pitch cause stall of the inboard regions of the blade (i.e. driving region), hence torque equilibrium is not possible. As a result, rotor speed decreases rapidly, thrust decreases and velocity of descent increases. Comparison of the autorotational diagram¹² and output from the AMRA model (see Fig.19) shows that the simulation correctly estimates critical blade pitch to be about 0.2rad.

In the case of negative value of blade fixed incidence angle, the rotor speed is significantly higher than for zero or small positive value of the angle and torque equilibrium is established. However, this configuration of autogyro rotor is not practical since speed of descent during steady autorotation is very high.

ii) Blade twist

A parametric study was performed to establish the influence of blade twist. The conclusions are very similar to those obtained during the study dealing with varying blade incidence angle - i.e.

steady autorotation is possible only for moderate values of blade twist. However, the limiting value of linear blade twist is higher as it affects mainly the outboard part of the blade where inflow angle is relatively small (see Fig.21). It can be noted that, in analogy with the study of the effect of blade incidence angle, negative twist of the blade increases both rotor speed and velocity of descent.

Provided that rotor speed is high enough and the rotor blade is in stable configuration, autorotation is a very stable flight regime. Simulations were carried out for several different magnitudes of twist disturbance to study the ability of a rotor in autorotation to recover from a gust. The effect of a gust was modelled as a step input in collective pitch. Figures 22 and 23 depict clearly that, if the blade is in stable configuration, coupling between rotor speed, blade twist and flap return have strong auto-stabilizing characteristics. The rotor speed recovers even if the magnitude of the disturbance is relatively high. Computations have also demonstrated that the rotor is not able to reach steady autorotation if rotor speed is too low. The highest twist deflection leads to significant decrease of rotor speed that results in stall of significant part of the blade. Stable autorotation is not re-established since the lift drops and drag increases considerably behind the stall point.

iii) Blade tip mass

Blade tip mass is frequently used to increase moment of inertia of gyroplane rotor blades. Higher moment of inertia further improves the stability of autorotation and therefore decreases probability of abrupt loss of rotor speed due to a gust or poor piloting. Computation for several different values of blade tip mass were undertaken to establish how sensitive autorotative state is to changes in this parameter. The concentrated mass was placed at the local elastic axis in order not to affect blade pitch dynamics. The outcome of the simulations is shown in Fig.24. It can be seen that the tip mass increases rotor speed as anticipated.

Results of the simulations have demonstrated that the effect of coupling between blade twist and rotor speed is very significant due to strong influence of blade incidence angle on both torque and thrust of the blade. Therefore, the conclusion can be drawn that the value of blade torsional stiffness is the key parameter of any gyroplane blade design. Together with chord-wise location of the elastic axis and centre of gravity, flexural stiffness has the decisive effect on aeroelastic stability of a rotor in autorotation. Further investigations have shown that blade flexural stiffness plays rather inferior role in this case due to centrifugal stiffening.

4.3. Stability boundary

In order to investigate rotor stability boundary in torsion, simulations for various torsional stiffness, chord-wise positions of centre of gravity (CG) and chord-wise positions of elastic axis (EA) were carried out.

The results of the simulations have revealed that low torsional stiffness of the blade leads to an aeroelastic instability (flutter) that comes through as coupled rotor speed / pitch / flap oscillations (see Fig.25 and 26). These oscillations result in catastrophic decrease of rotor speed as is shown in Fig.26. Reduction of rotor speed from a steady value to zero takes only few seconds and the speed of descent increases to unacceptable value during this time. This type of flutter seems to be unique for rotor in autorotation since it differs from both helicopter rotor flutter and flutter of a fixed wing.

It can be seen from figures 27 and 28 that position of CG aft EA is destabilizing, which agrees both with theory of aeroelasticity and experiments. Chord-wise position of CG seems to have much stronger influence on the stability of autorotation than chord-wise position of EA. It is probably caused by the fact that the offset of aerodynamic centre (AC) from EA (i.e. the arm of forcing torsional moment) is another factor influencing stability the shape of boundary and it is a function of chord-wise location of EA.

$$\begin{aligned} \mathcal{Y}_c &= \mathcal{Y}_{AC} - \mathcal{Y}_{EA} \\ \mathcal{Y}_g &= \mathcal{Y}_{CG} - \mathcal{Y}_{EA} \end{aligned} \tag{4.3}$$

All results of the investigations can be summarised in 3-D chart that comprises change of the stability boundary due to both variation of CG position and variation of EA position (see Fig. 29 and 30).

5. SIMULATION OF AUTOROTATIVE FORWARD FLIGHT

Since gyroplanes operate mostly in forward flight regime, modelling of forward autorotative flight represents the key task in investigation of aeroelastic behaviour of a gyroplane rotor blade. In comparison to the simulation of axial autorotative flight, simulation of forward flight in autorotation induces some complication. Both direction and value of the inflow velocity are functions of azimuth if horizontal speed is not zero (see equations). This means that there is no torque equilibrium during steady forward flight and the value of torque oscillates around the zero value (see Fig.31). The amount of vibrations induced by the rotor blade during steady forward flight is therefore significantly higher than in axial descent. In addition, free-stream velocity at the advancing side of the rotor disc is higher, and thus the values of the forcing moments are higher too. It can be expected that gyroplane rotor blade in the forward flight regime is more prone to undergo aeroelastic instability than the same blade during axial autorotative flight.

i) Chord-wise position of CG and EA

Computations carried out with the aid of the latest version of the AMRA model have shown that the rotor suffers of aeroelastic instability if CG lies aft EA. The model has also predicted that fixed incidence angle of the blade (collective pitch) has very strong influence on shape of torsional stability boundary. In order to gain more knowledge about the problem, parametric study focused on the effect of position of blade CG and EA was performed. Computations for EA at 35%c and different chord-wise locations of CG and values of torsional stiffness k_θ were undertaken. Since most of parameters in forward autorotative flight have harmonic behaviour, the results are presented in the form of boundaries of their trends. This approach allows comparison of multiple data sets in one plot. Figures 31 and 32 show an example of results of the simulations obtained from forward autorotative flight in stable configuration ($V_h = 50\text{m/s}$, CG ahead of EA). Comparison of time behaviours of rotor speed of a rotor blade in unstable configuration (CG at 45%c and EA at 35%c) during autorotative axial descent and forward flight is depicted in Fig.33. Blade incidence angle is set to 0.04rad for both axial flight and forward flight. Note that in the case of axial descent, the instability occurs at much lower torsional stiffness than during forward flight. In forward flight, instability develops even for value of realistic torsional stiffness obtained during experimental measurements of blade structural properties ($k_\theta = 1600\text{N.m}^2/\text{rad}$). Figures 34 - 37 compare estimations of the behaviour of the rotor during forward flight for zero blade incidence angle and blade incidence angle $\theta_c = 0.04\text{rad}$. The influence of blade incidence in forward autorotative flight seems to be even stronger than during axial descent. Stability boundaries obtained for forward flight regime are given in Fig. 35 and 37. Corresponding data for autorotative vertical flight can be found in Fig.27. The Results of the simulations clearly show that the auto-stabilising effect of pitch-flap-rotor speed coupling is relatively strong during axial descent, but is suppressed by flow-induced oscillations in forward flight.

ii) Blade fixed incidence angle

Figures 38 and 39 show results of a series of simulations to investigate the effect of blade incidence angle alone (without change of chord-wise location of CG). Again, blade incidence angle seems to have a strongly destabilizing effect. Another set of calculations was carried out for different values of horizontal speed. It can be seen from Fig.40 and 41 that both flapping and torsion of the blade increases with rise of horizontal speed. Rotor speed, however, does not change since the configuration of the rotor remains unchanged.

6. CONCLUSIONS

An aeromechanical model of a gyroplane rotor *AMRA* was developed and used in predicting the aeroelastic behaviour of a rotor. Both regimes were investigated – autorotative axial flight (vertical descent) and forward flight in autorotation. Simulations have shown that autorotation is a complex aeromechanical process with auto-stabilizing characteristics. It was found that blade twist / rotor speed coupling has major effect on stability of autorotation when the rotor is in a stable configuration.

In order to obtain input parameters for the structural model of the blade, a series of experimental measurements were carried out. Blade mass distribution, position of elastic axis, span-wise distribution of CG and torsional and flexural stiffness was determined during the experiments.

Results from the *AMRA* model were verified and found to be in a good agreement with both existing theory of aeroelasticity and experimental measurements. Several parametric studies were performed so as to gain more knowledge on the effect of blade geometry and structural properties on performance of the rotor during autorotation.

Occurrence of a type of flutter that is unique for autorotating rotor was discovered during simulation of unsteady axial descent in autorotation. This aeroelastic instability is driven by blade pitch / flap / rotor speed coupling and differs from both flutter of a helicopter rotor and flutter of a fixed wing. The instability results in catastrophic decrease of the rotor speed and significant increase of speed of descent.

Preliminary results of simulation of gyroplane rotor in forward flight were obtained and analysed. The *AMRA* model suggests that positive blade twist has adverse effect on performance of the rotor during autorotative forward flight. Very low positive or zero fixed blade incidence angle and moderate amount of blade tip mass seem to be beneficial for performance of a rotor in autorotation. Low negative value of blade linear twist can also improve its behaviour as it decreases angle of attack of the outboard part of the blade which is the source of negative torque during autorotation.

More powerful structural model of gyroplane blade that will utilise finite element method (FEM) will be developed in the next stage of the project. It will be coupled with RASCAL advanced rotor blade aerodynamic model developed by Dr Houston from Department of Aerospace Engineering, University of Glasgow.²⁰

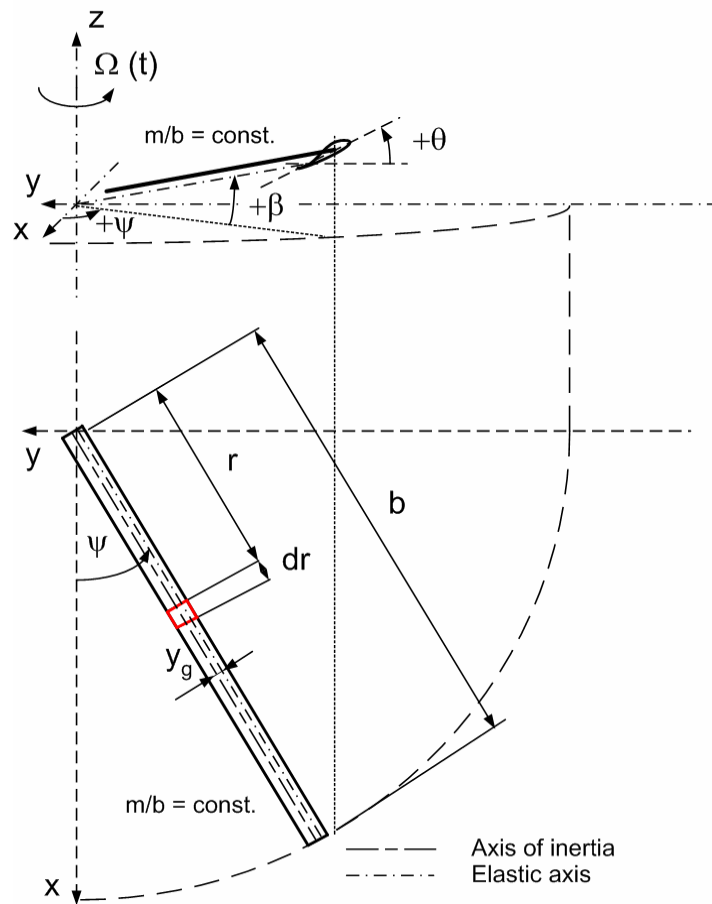


Figure 1 – General arrangement of the autogiro rotor blade model.

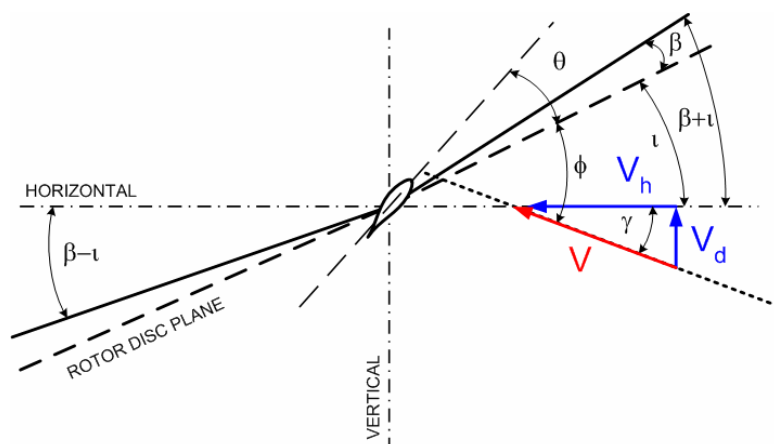


Figure 2 – Relation of blade twist, flap and inflow angle

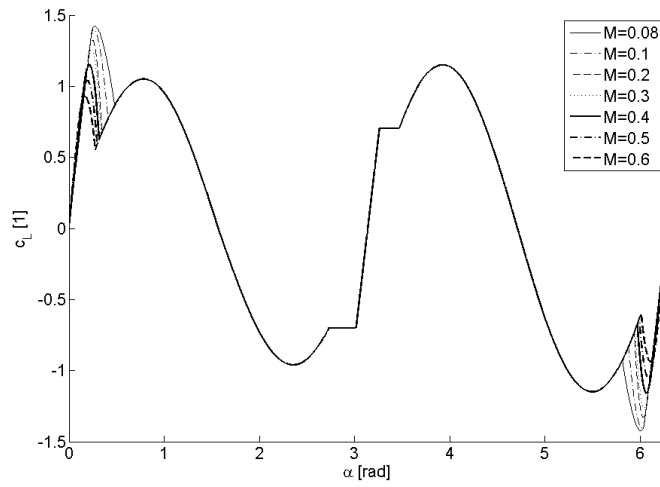


Figure 3 – Trends of NACA 0012 lift coefficient obtained for different values of Mach number.

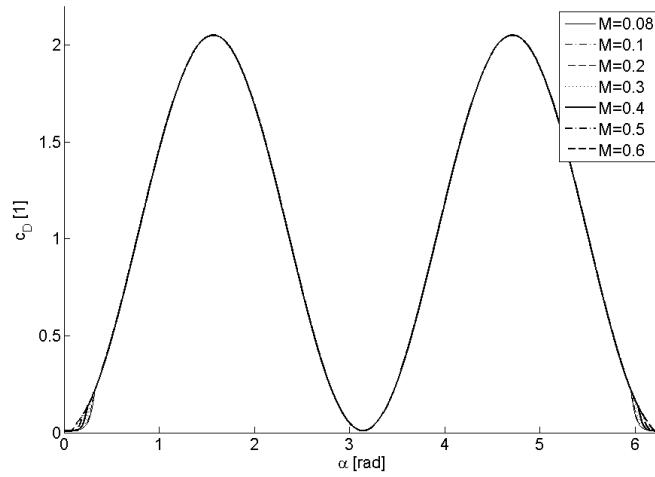


Figure 4 - Trends of NACA 0012 drag coefficient obtained for different values of Mach number.

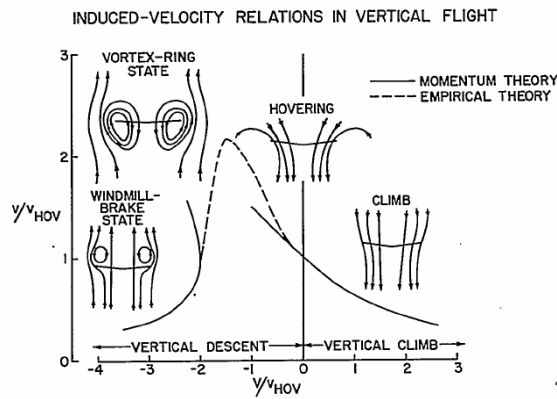


Figure 5 – Induced velocity relations in vertical flight (speed of climb on the x-axis, induced velocity on the y-axis).
Reproduced from Ref. 23.

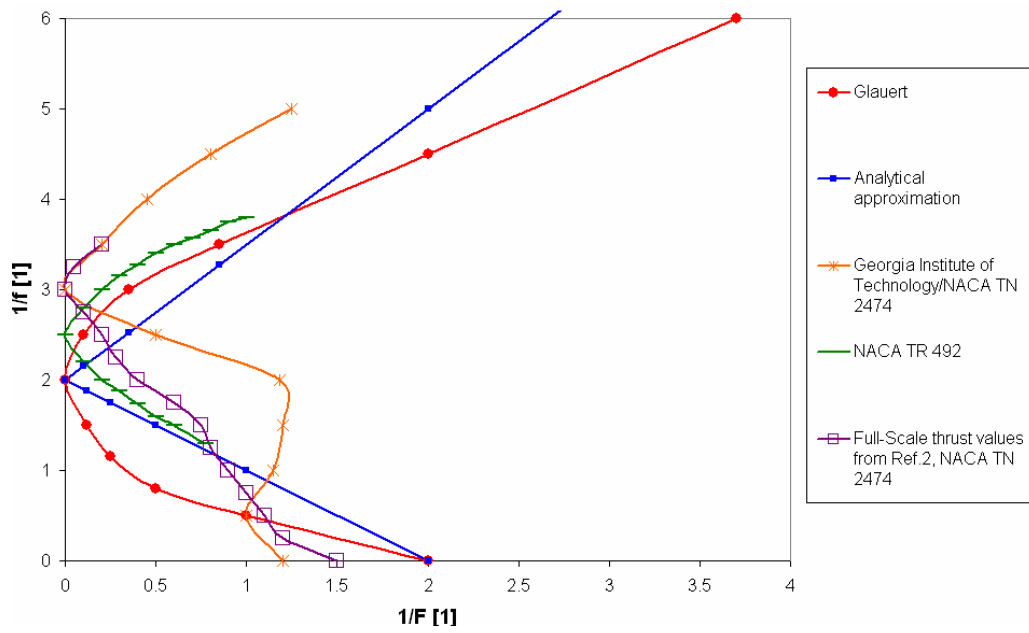


Figure 6 – Experimental data on relation of $1/f$ and $1/F$.

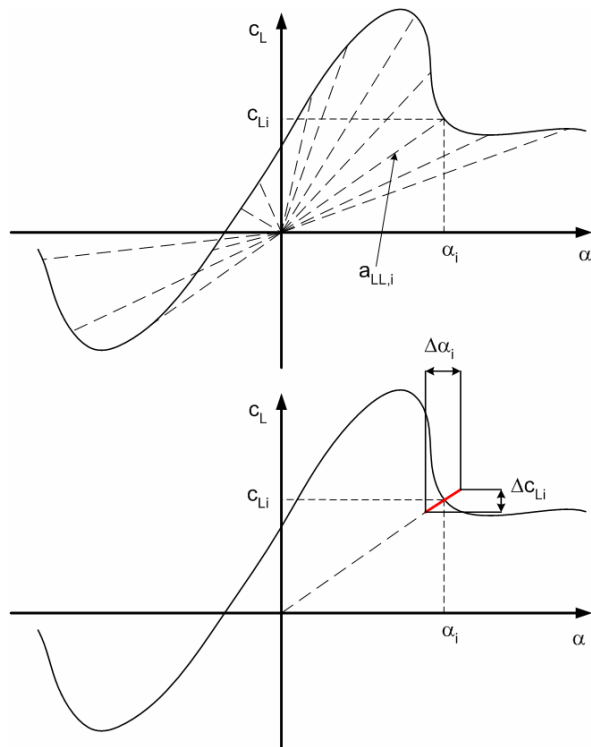


Figure 7 – Definition of 'local' lift curve slope.

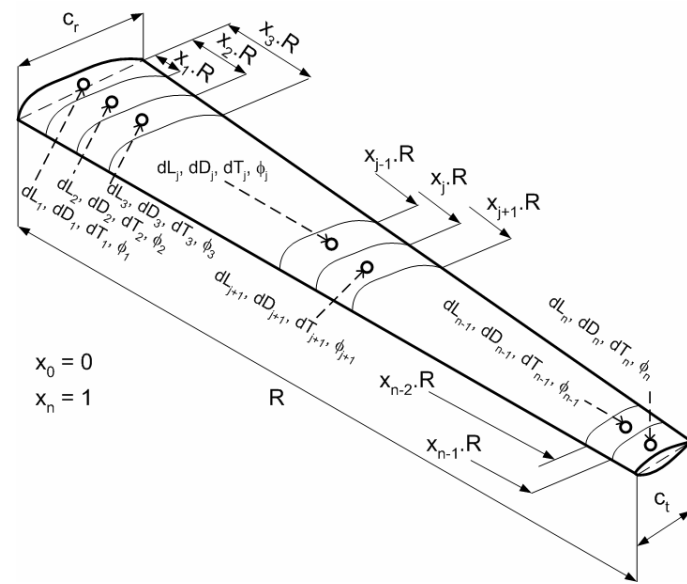


Figure 8 – Arrangement of the blade model.

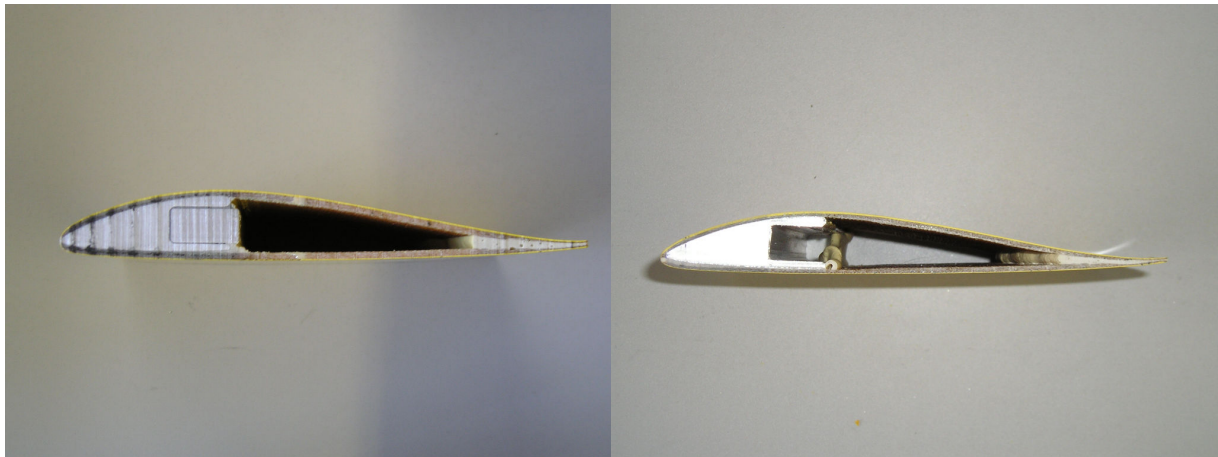


Figure 9 – Internal structure of the rotor blade from Montgomerie-Parsons research autogiro. Left section comes from the root of the blade while the right one was located close to the tip of the rotor blade.

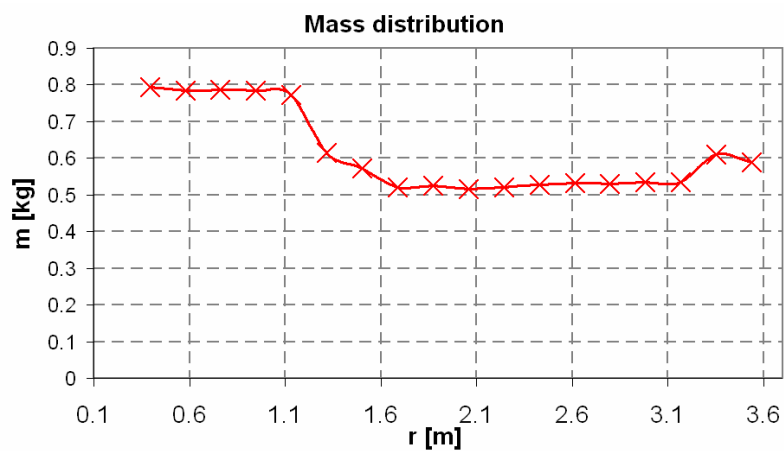


Figure 10 – Span-wise mass distribution of the blade. The total weight of one blade was 11.95kg.

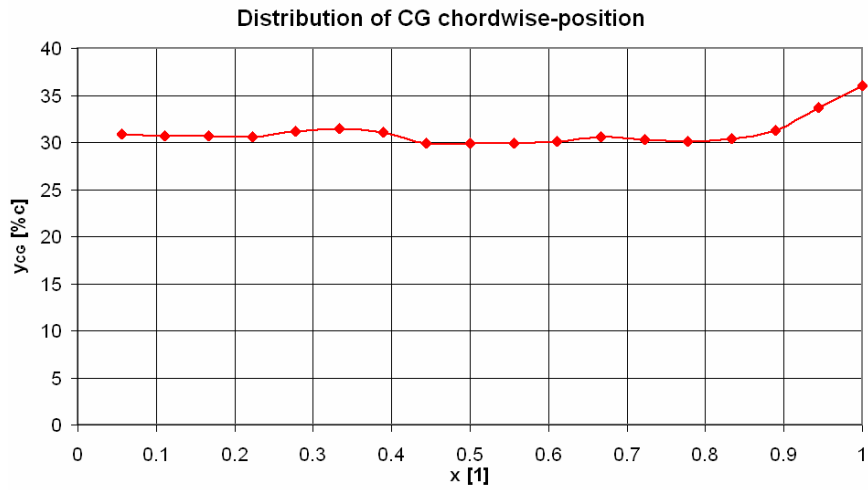


Figure 11 – Span-wise distribution of blade CG.



Figure 12 – Arrangement of the experimental measurements of EA position and torsional stiffness of the blade.

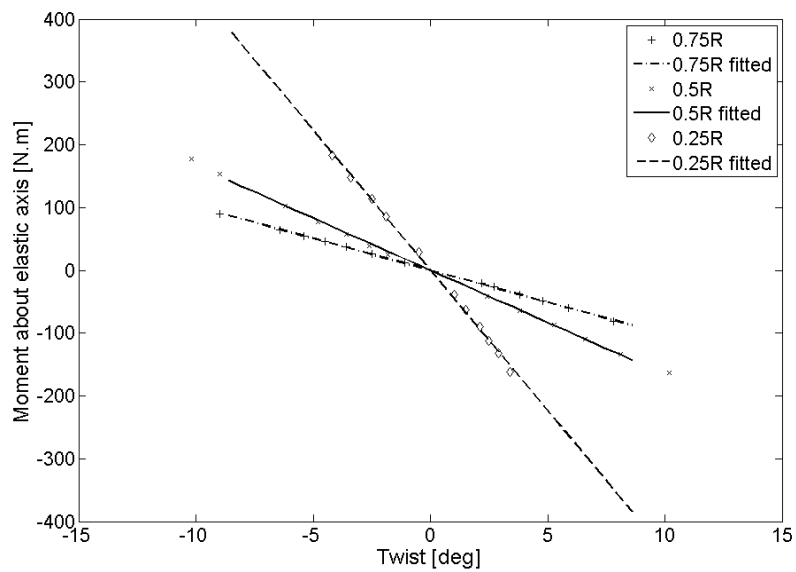


Figure 13 – Dependence of blade twist upon torsional loading at three span-wise stations.

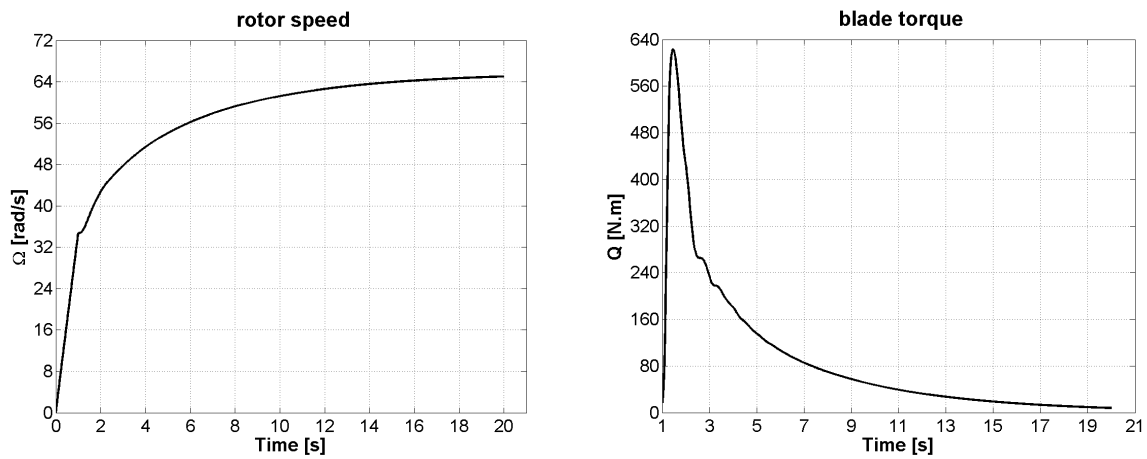


Figure 14 – Stabilization of rotor speed and corresponding torque equilibrium during steady axial autorotative flight.

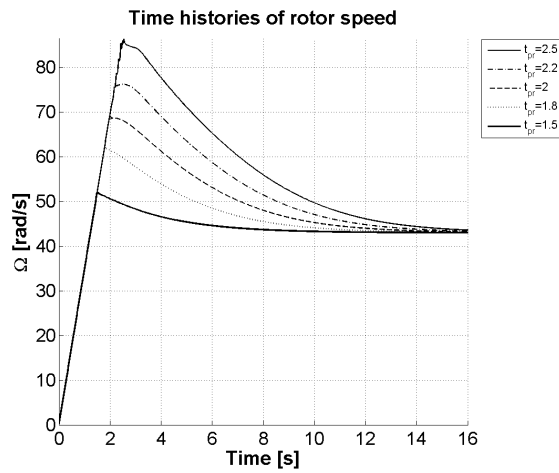


Figure 15 – Time behaviour of rotor speed for different lengths of pre-rotation.

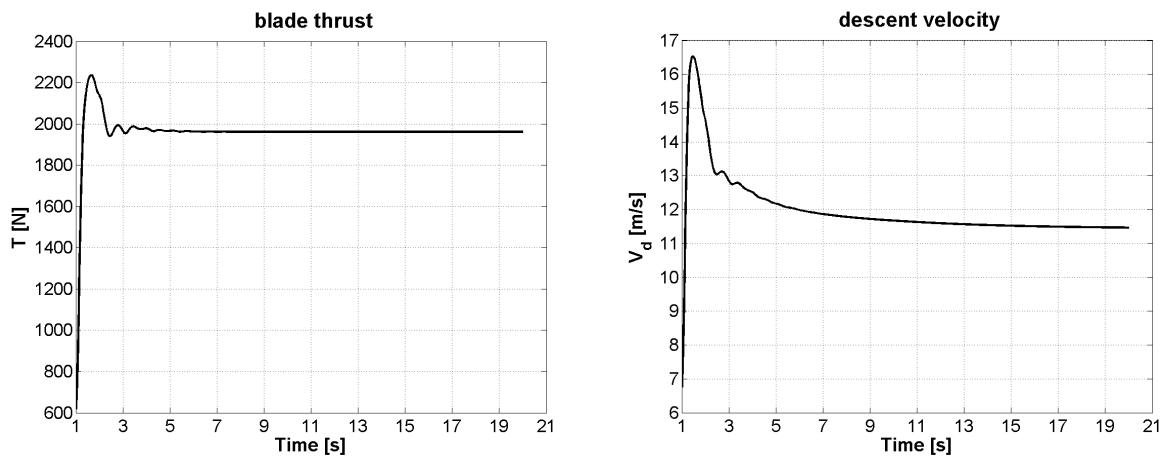


Figure 16 – Trends of thrust and speed of descent during steady autorotative descent. Plot on the left shows thrust of one blade only, so the value of thrust has to be multiplied by two to obtain total rotor thrust (the rotor is two-bladed).

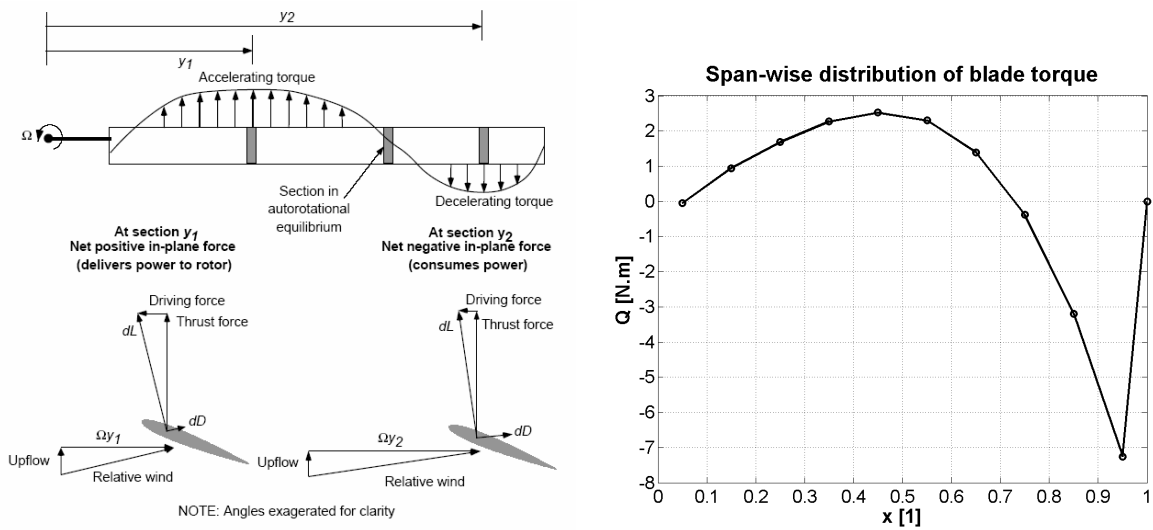


Figure 17 – Span-wise distribution of torque during steady autorotation. The right-hand side figure was published in Ref. 14 and Ref. 16.

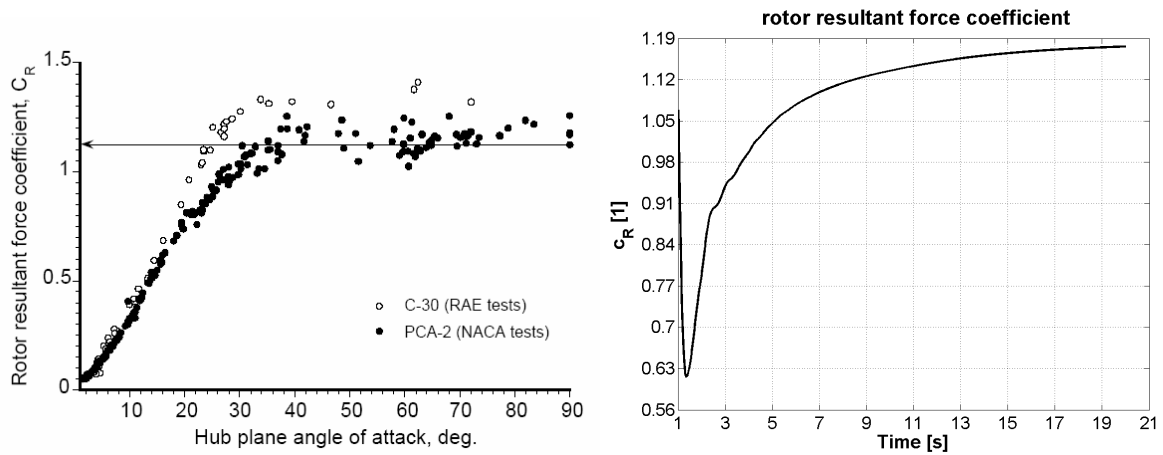


Figure 18 – Comparison of values of resultant force coefficient as a function of rotor disc angle of attack obtained by experimental flight measurements (left) and value of c_R predicted by the simulation for axial flight (i.e. $\alpha_D = 90\text{deg}$) and zero blade incidence angle.

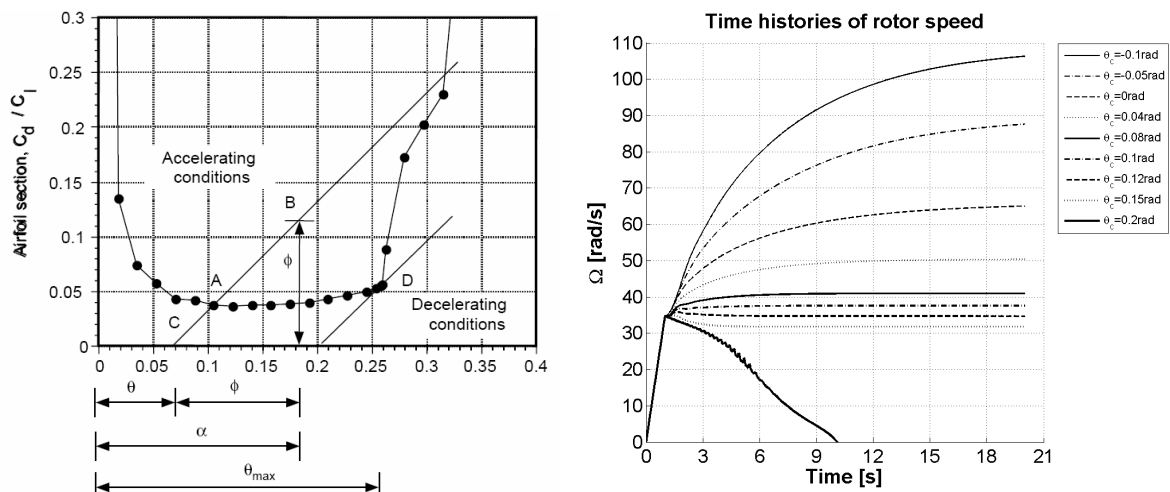


Figure 19 – Comparison of autorotational diagram that was introduced by Vimperis¹⁴ (right) and results of the simulation.

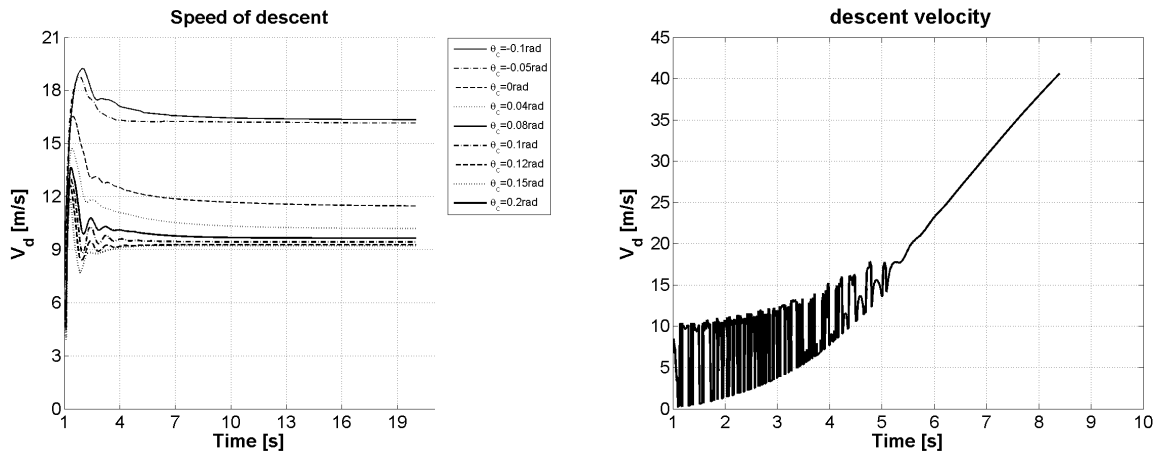


Figure 20 – Rotor speeds and velocities of descent for several collective pitch settings; stable configurations on the left. Plot on the right-hand side shows rapid increase of speed of descent that occurs when the configuration is unstable. As it can be seen from the previous figure, rotor speed drops to zero in 9 seconds.

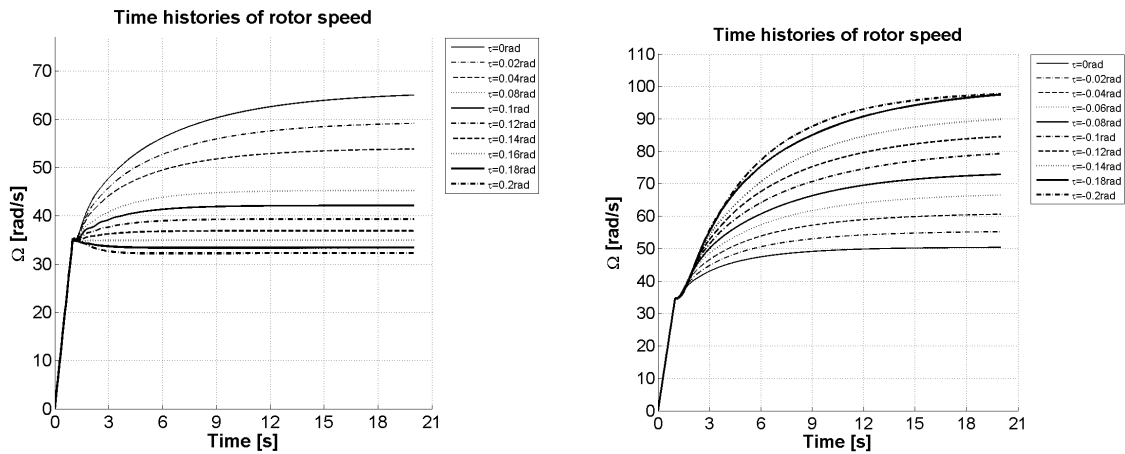


Figure 21 – Trends of rotor speed for several values of positive linear blade twist (left) and negative linear blade twist (right).

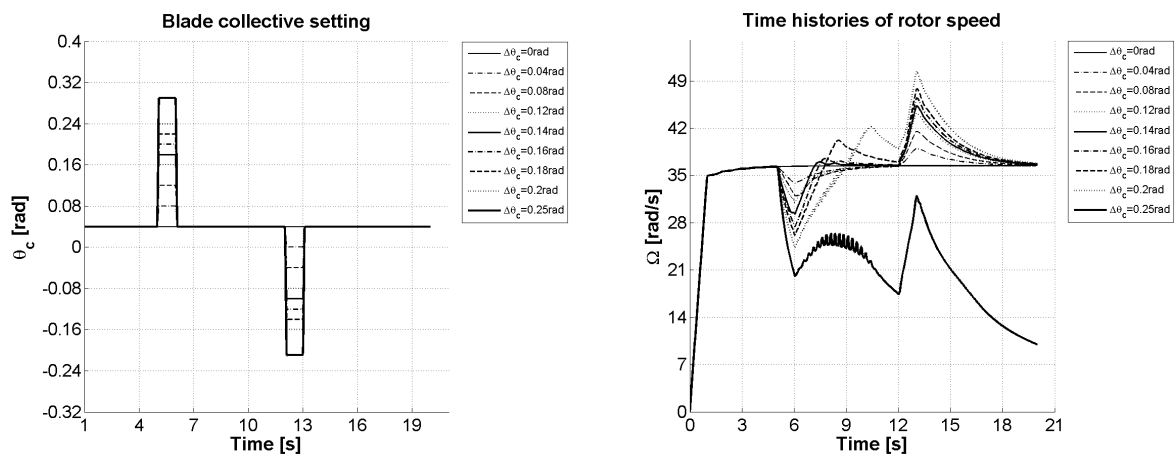


Figure 22 – Three different types of twist disturbance that were used during testing of the model.

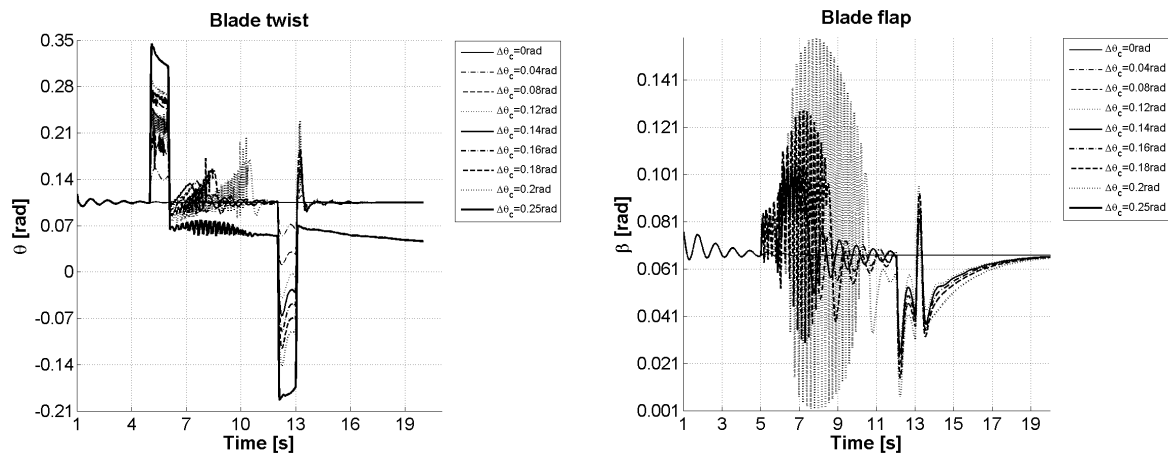


Figure 23 – Recovery of rotor speed after three different pitch perturbations.

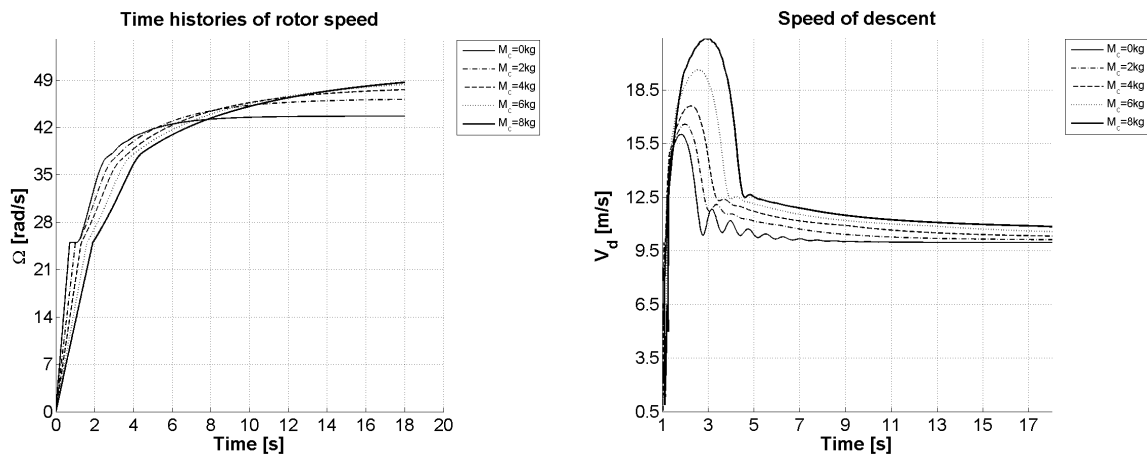


Figure 24 – Trends of rotor speed and speed of descent obtained for five different values of blade tip mass.

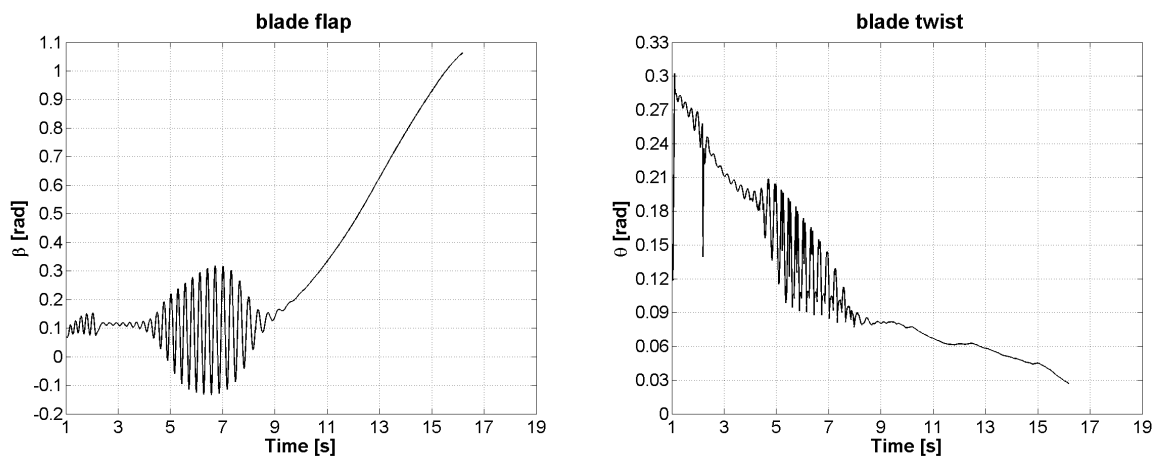


Figure 25 – Flap oscillation during unstable axial autorotative flight. Calculated for $k_\theta = 300\text{N}\cdot\text{m}^2/\text{rad}$.

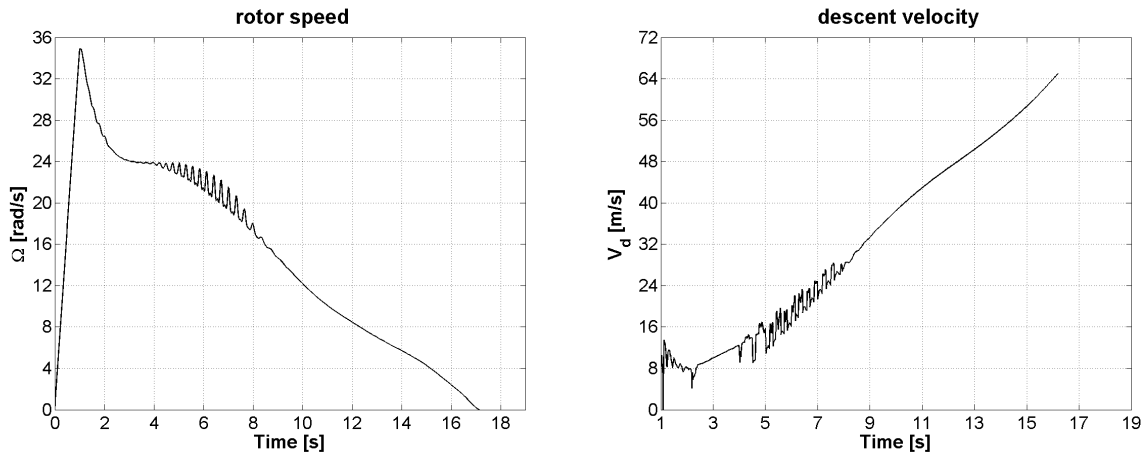


Figure 26 – Oscillation in pitch that occur during unstable axial autorotative flight. Calculated for $k_\theta = 300 \text{ N}\cdot\text{m}^2/\text{rad}$.

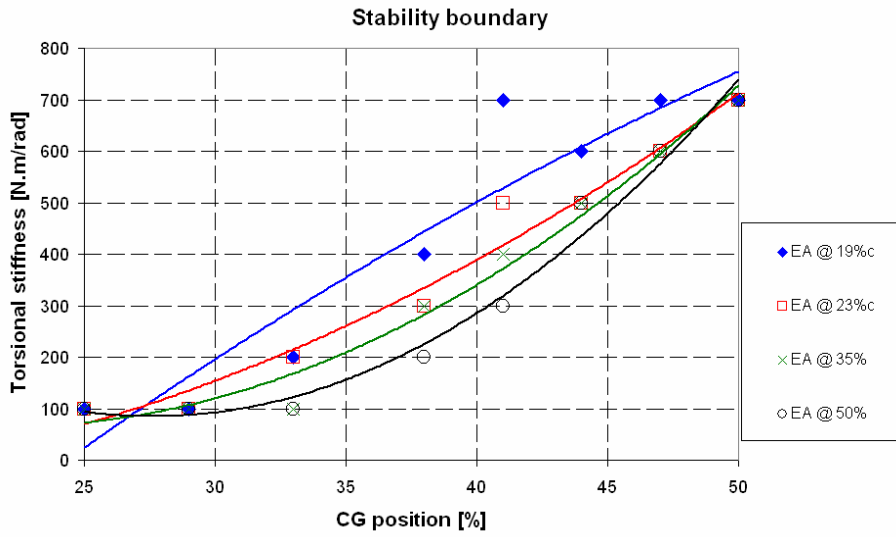


Figure 27 – Stability boundaries in torsion for different chord-wise positions of CG and EA.

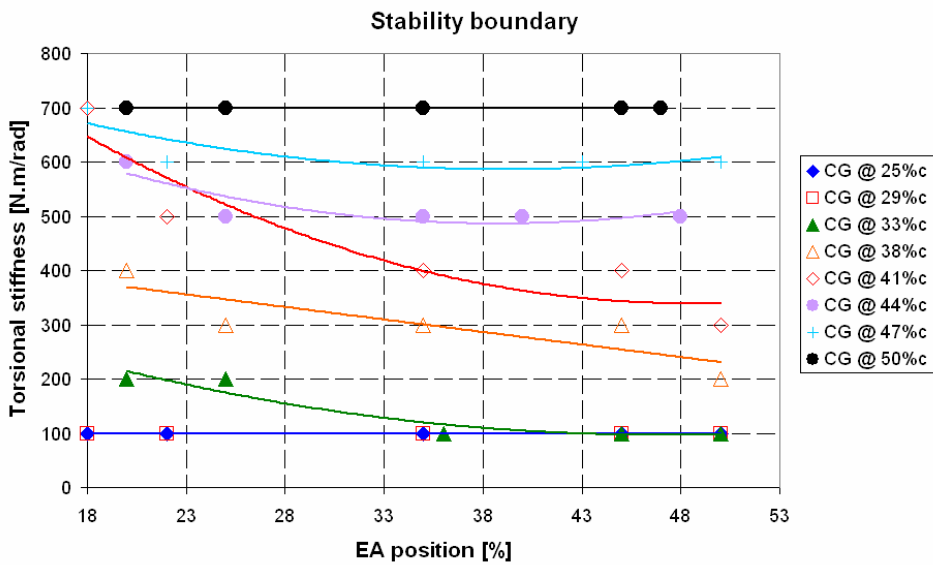


Figure 28 - Stability boundaries in torsion for different chord-wise positions of CG and EA.

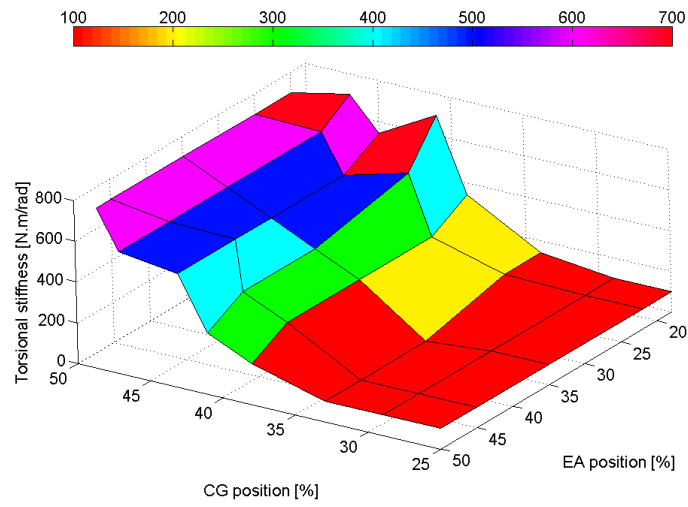


Figure 29 – Graphical interpretation of the parametric study on torsional stability boundary of a rotor in autorotative axial flight.

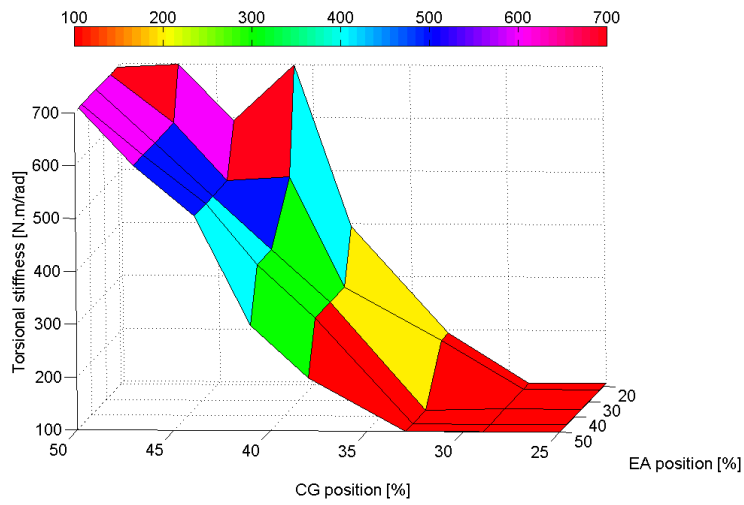


Figure 30 - Graphical interpretation of the parametric study on torsional stability boundary of a rotor in autorotative axial flight.

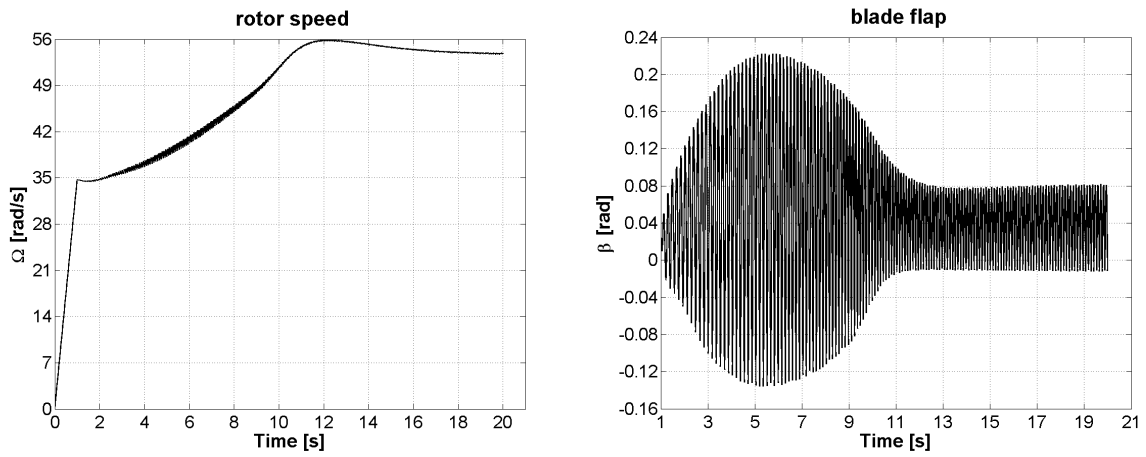


Figure 31 – Rotor speed and blade flap angle in stable forward flight.

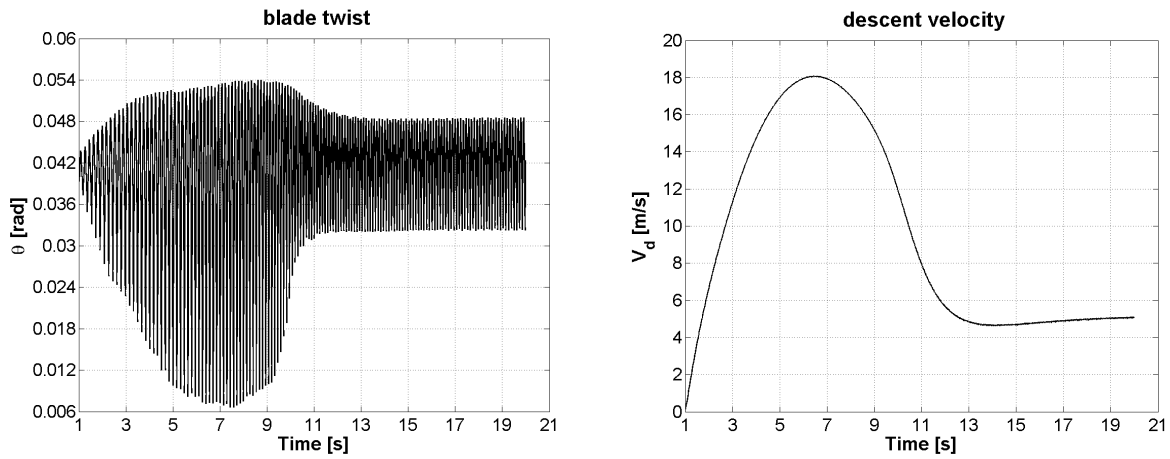


Figure 32 – Blade twist and speed of descent of an autogiro during stable forward flight.

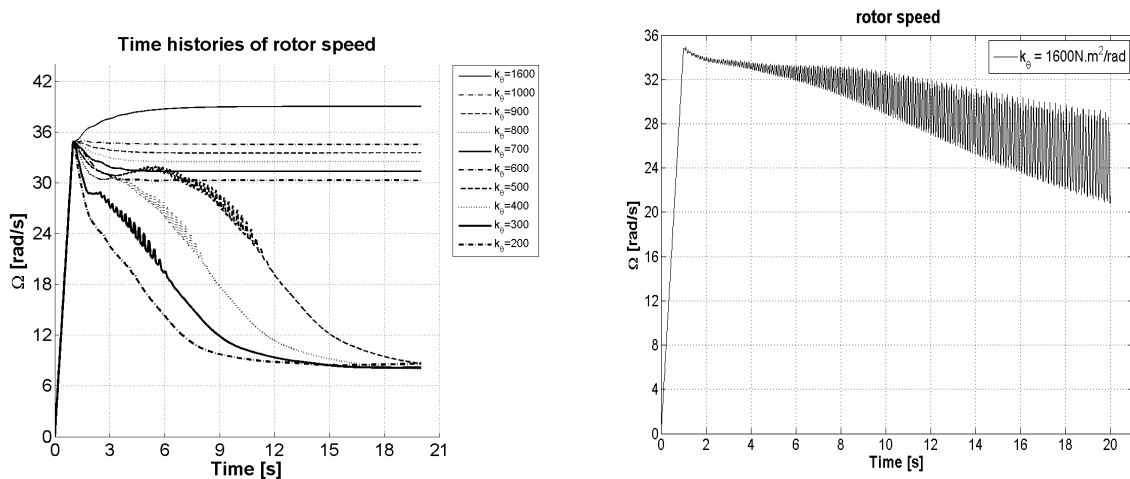


Figure 33 – Comparison of aeroelastic behaviour of a gyroplane rotor blade in axial descent (left) and forward flight (right). Both calculations were accomplished for the blade in unstable configuration (CG aft EA).

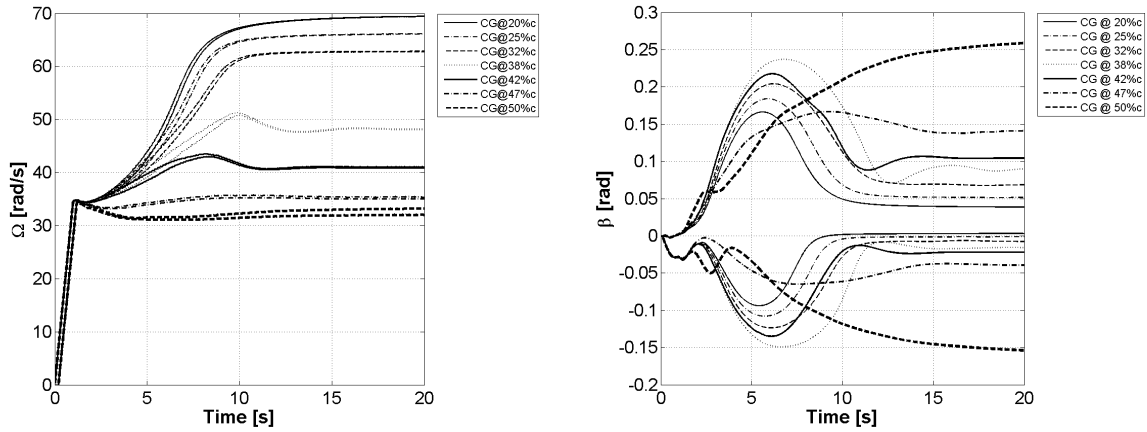


Figure 34 - Behaviour of rotor speed and flapping angle during autorotative forward flight for zero blade incidence angle and different chord-wise positions of CG. The torsional stiffness is $1600\text{N}\cdot\text{m}^2/\text{rad}$.

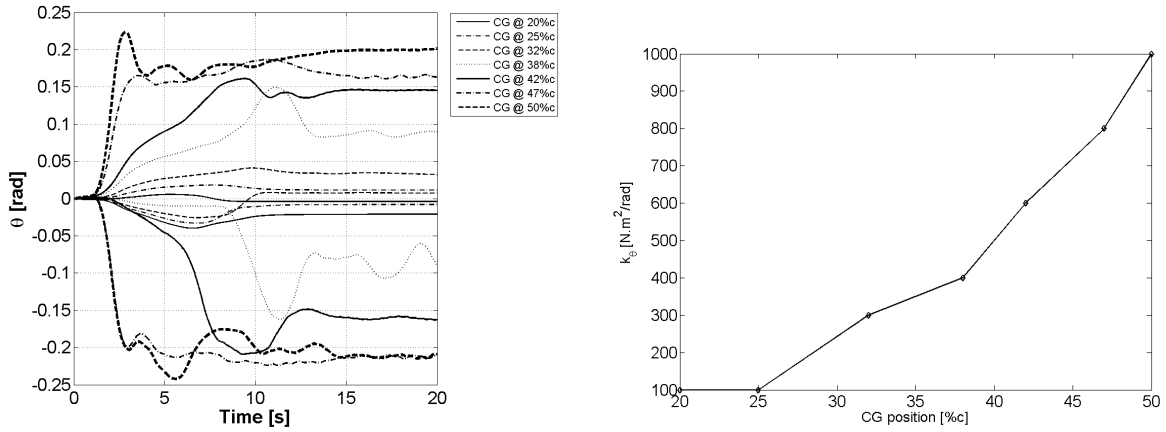


Figure 35 - Behaviour of rotor speed and flapping angle during autorotative forward flight for zero blade incidence angle and different chord-wise positions of CG. The torsional stiffness is $1600\text{N}\cdot\text{m}^2/\text{rad}$. The right-hand side plot shows the stability boundary in torsion for the given blade incidence angle.

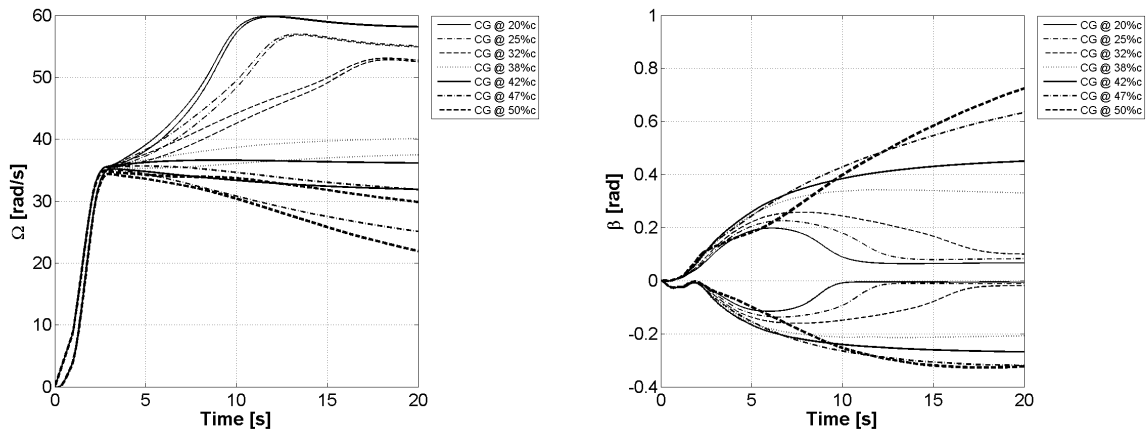


Figure 36 - Behaviour of rotor speed and flapping angle during autorotative forward flight for blade incidence angle of 0.04 rad and different chord-wise positions of CG. The torsional stiffness is $1600\text{N}\cdot\text{m}^2/\text{rad}$.

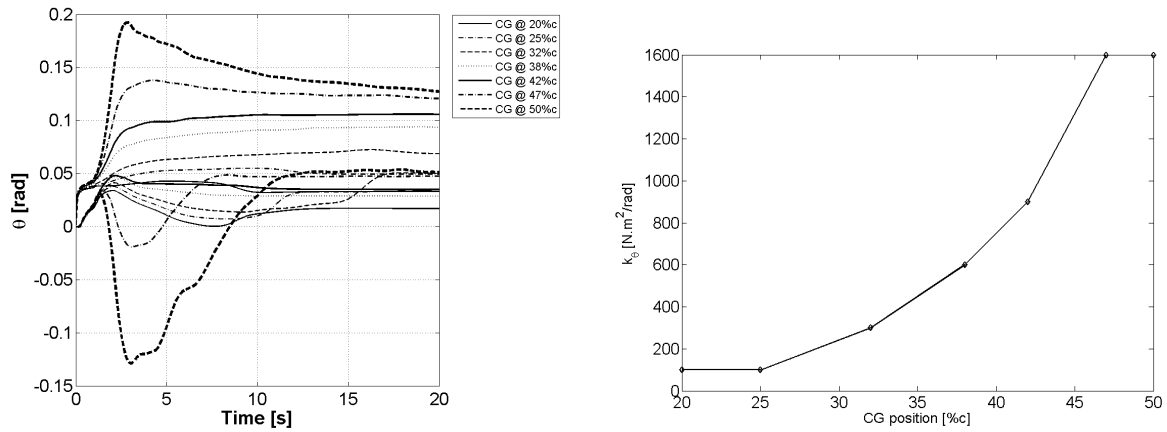


Figure 37 - Behaviour of rotor speed and flapping angle during autorotative forward flight for blade incidence angle of 0.04rad and different chord-wise positions of CG. The torsional stiffness is 1600N.m²/rad. The right-hand side plot shows the stability boundary in torsion for the given blade incidence angle.

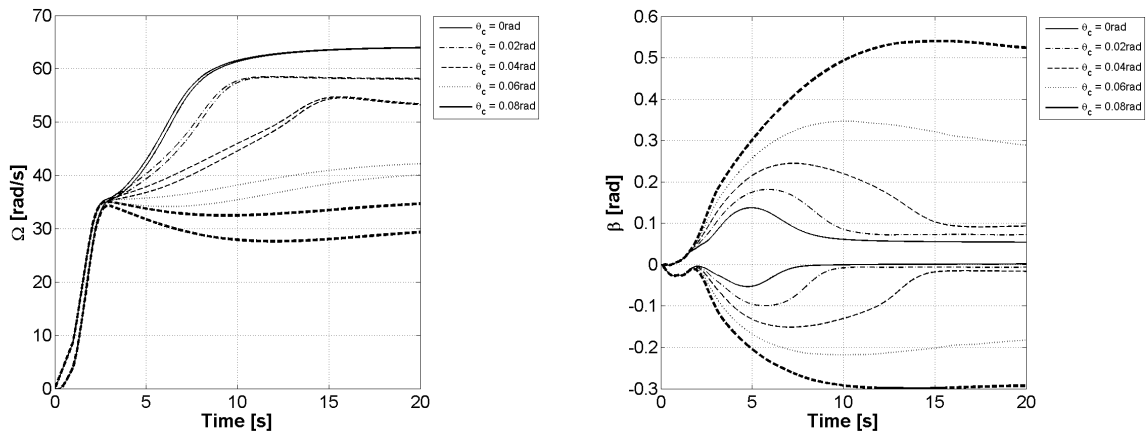


Figure 38 – The effect of blade incidence angle (collective pitch) on aeroelastic behaviour of a gyroplane rotor in forward flight.

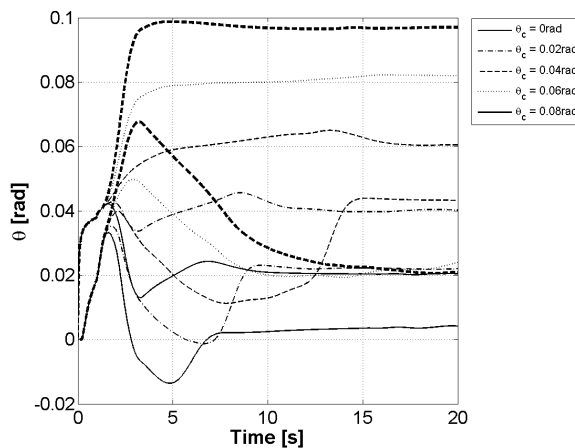


Figure 39 – Twist of the blade obtained for different values of blade incidence angle (i.e. collective pitch).

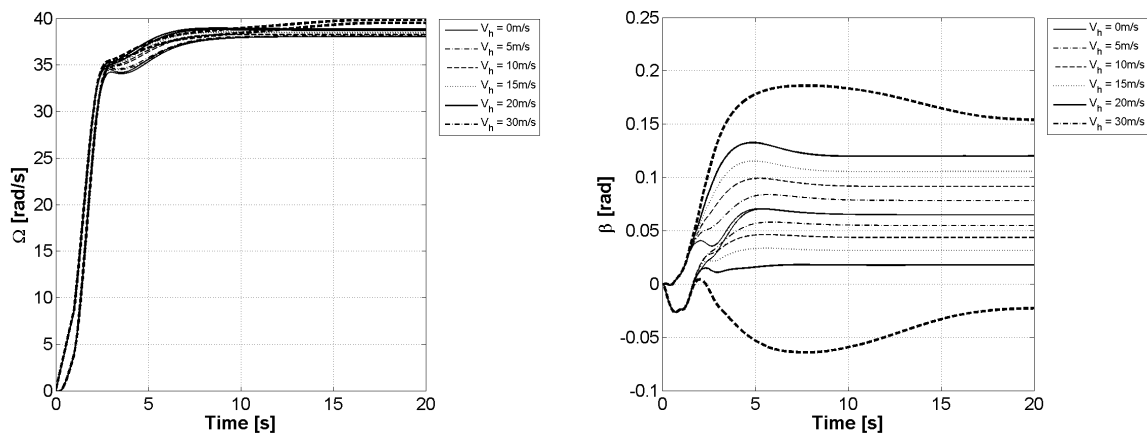


Figure 40 – The effect of the value of forward speed on rotor speed and flapping angle of the blade.

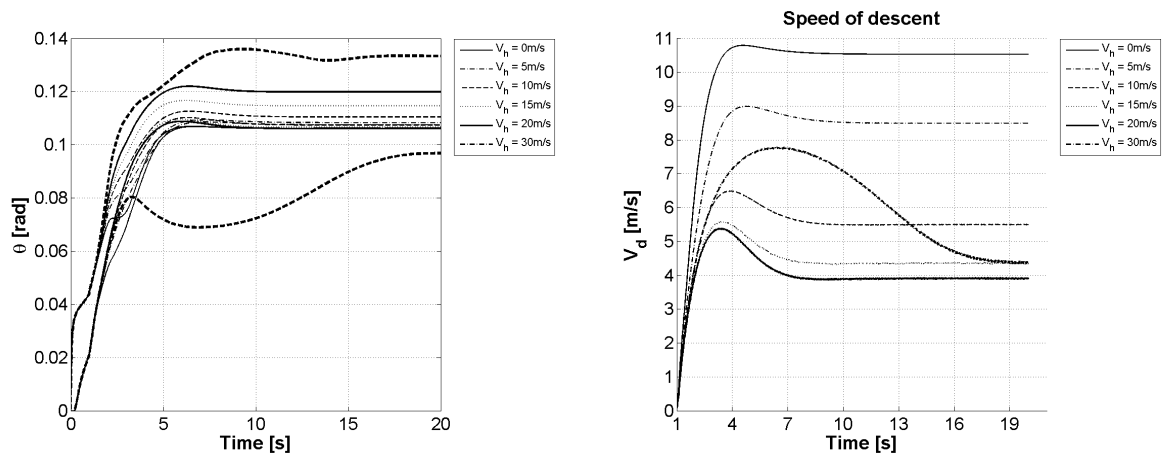


Figure 41 – Blade twist and values of speed of descent for different values of forward speed.

7. REFERENCES

- [1] Thomson, D.G., Houston, S.S., Spathopoulos, V. M., “Experiments in Autogiro Airworthiness for Improved Handling Qualities”, Journal of American Helicopter Society, Pg. 295, No. 4, Vol. 50, October 2005.
- [2] Houston, S. S., “Longitudinal Stability of Gyroplanes”, The Aeronautical Journal, Vol. 100 (991), 1996, pp. 1-6.
- [3] Houston, S. S.: “Identification of Autogiro Longitudinal Stability and Control Characteristics”, Journal of Guidance, Control and Dynamics, Vol. 21, No. 3, 1998, pp. 391-399.
- [4] Coton, F., Smrcek, L., Patek, Z., “Aerodynamic Characteristics of a Gyroplane Configuration”, Journal of Aircraft, Vol. 35, No. 2, 1998, p. 274 – 279.
- [5] Prouty, R. W., “Helicopter Performance, Stability and Control”, Robert E. Krieger Publishing Co., Malabar, FA, USA, 1990.

- [6] Sheldahl, R. E., Klimas, P. C., “Aerodynamic Characteristics of Seven Aerofoil Sections Through 180 Degrees Angle of Attack for Use in Aerodynamic Analysis of Vertical Axis Wind Turbines”, SAND80-2114, Sandia National Laboratories, Albuquerque, New Mexico, USA, 1981.
- [7] Nikolsky, A.A., Seckel, E., “An Analytical Study of the Steady Vertical Descent in Autorotation of Single-Rotor Helicopters”, NACA TN 1906, Washington, 1949.
- [8] Houston, S. S., “Modelling and Analysis of Helicopter Flight Mechanics in Autorotation”, *Journal of Aircraft*, Vol. 40, No. 4, 2003.
- [9] Spathopoulos, V. McI., “The Assessment of a Rotorcraft Simulation Model in Autorotation by Means of Flight Testing a Light Gyroplane”, PhD Thesis, Department of Aerospace Engineering, University of Glasgow, 2001.
- [10] Leisman, J.G., “Principles of Helicopter Aerodynamics”, Cambridge University Press, 2nd Edition, 2006, pp.428-431. ISBN 0-521-85860-7
- [11] Wheatley, J.B., “An Aerodynamic Analysis of the Autogiro Rotor with a Comparison between Calculated and Experimental Results,” NACA TR 487.
- [12] Leisman, J.G., “The Development of the Autogiro: A Technical Perspective”, *Journal of Aircraft*, Vol. 41, (2), 2004, pp. 765-781.
- [13] Bramwell, A. R. S. et al, “Bramwell’s Helicopter Dynamics”, 2nd edition, Butterworth-Heinemann, 2001. ISBN 0-7506-5075-3
- [14] Sissingh, G., “Contribution to the Aerodynamics of Rotating-Wing Aircraft,” NACA TM 921
- [15] Wheatley, J.B., “The Aerodynamic Analysis of the Gyroplane Rotating-Wing System,” NACA TN 492, Langley Memorial Aeronautical Laboratory, 1934.
- [16] www.cyberiad.net/foildata.htm The data were synthesized from a combination of experimental results published in [20] and computer calculations.
- [17] Wheatley, B., Bioletti, C., “Wind-Tunnel Tests of a 10-foot-diameter Gyroplane Rotor”, NACA TR 536.
- [18] Wheatley, B., Bioletti, C., “Wind-Tunnel Tests of a 10-foot-diameter Gyroplane Rotors”, NACA TR 552.
- [19] Wheatley, B., Hood, M. J., “Full-Scale Wind-Tunnel Tests of a PCA-2 Autogiro Rotor”, NACA TR 515.
- [20] Houston, S.S., “Validation of a non-linear individual blade flight dynamics model using a perturbation method”, *The Aeronautical Journal of the Royal Aeronautical Society*, Vol.98, No.977, Aug-Sep. 1994.
- [21] Carpenter, P.J., “Lift and Profile-drag Characteristics of an NACA 0012 Airfoil Section as Derived from Measured Helicopter-rotor Hovering Performance”, NACA TN 4357, Langley Memorial Aeronautical Laboratory, Langley Field, VA, USA, 1958.
- [22] Wheatley, J.B., “An Aerodynamic Analysis of the Gyroplane Rotating-Wing System”, NACA TR 487, Langley Memorial Aeronautical Laboratory, Langley Field, VA, USA, 1934.
- [23] Wheatley, J.B., “An Aerodynamic Analysis of the Autogiro Rotor with a Comparison between Calculated and Experimental Results”, NACA TR 487.
- [24] Castles, W., Gray, R.B., “Empirical Relation Between Induced Velocity, Thrust and Rate of Descent of a Helicopter Rotor as Determined by Wind-Tunnel Tests on Four Model Rotors”, NACA TN 2474, Washington, 1951.
- [25] Brown, R. E., Houston, S. S., “CFD-based Simulation and Experiment in Helicopter Aeromechanics”, published at www.ae.ic.uk/research/rotorcraft/pubs.